Cortico-cortical feedback engages active dendrites in visual cortex

Mehmet Fişek[1,2], Dustin Herrmann[1,2], Alexander Egea-Weiss[1],
Matilda Cloves[1], Lisa Bauer[1], Tai-Ying Lee[1], Lloyd E. Russell[1]
& Michael Häusser[1]

1. Wolfson Institute for Biomedical Research, University College London, UK
2. These authors contributed equally

Correspondence to Michael Häusser: m.hausser@ucl.ac.uk or Mehmet Fişek: fisekm@gmail.com

Sensory processing in neocortex requires both feedforward and feedback information flow between cortical areas[1]. In feedback processing, higher-level representations provide contextual information to lower levels, and facilitate perceptual functions such as contour integration and figure-ground segmentation[2,3]. However, we have limited understanding of the circuit and cellular mechanisms that mediate feedback influence. Here, we use long-range all-optical connectivity mapping to show that feedback influence from the higher visual area LM to the primary visual cortex (V1) is spatially organized: when the source and target of feedback represent the same area of visual space, feedback is relatively suppressive, while when the source is offset from the target in visual space, feedback is relatively facilitating. Two-photon calcium imaging shows that this facilitating feedback is nonlinearly integrated in the apical tuft dendrites of V1 pyramidal neurons: retinotopically offset ('surround') visual stimuli drive local dendritic calcium signals indicative of regenerative events, and two-photon optogenetic activation of LM neurons projecting to identified feedback-recipient spines in V1 can drive similar branch-specific, local calcium signals. Our results show how neocortical feedback connectivity and nonlinear dendritic integration can together form a substrate to support both predictive and cooperative contextual interactions.

How does cortico-cortical feedback modify activity in the recipient circuit? To answer this question we must solve two problems. First, we must map feedback connectivity and second, we must understand how feedback is integrated on the single-cell level. A substantial proportion of feedback inputs innervate pyramidal cell apical dendrites in layer 1[1,4], where inputs are too distant to effectively influence the soma passively[5]. However, feedback may recruit the active properties of apical dendrites to compensate for this distance-dependent attenuation[5], providing a layer of nonlinear processing[6,7]. To map feedback connections and determine if they can drive active dendritic processes we focused on primary visual cortex (V1) and one of its prominent feedback sources: the lateral-medial higher visual area (LM), considered the mouse homolog to primate V2[8]. We studied layer 5 intratelencephalic (IT) neurons, which project to other cortical areas[9], possess apical dendrites capable of intrinsic electrogenesis[10] and can be targeted using the transgenic mouse line Tlx3-Cre[9].

Circuit organization of feedback

Feedback projections from higher visual areas to any given location in V1 cover a region of visual space much larger than the size of individual receptive fields[11,12] and target excitatory as well as inhibitory neurons[13]. Consistent with this, in vivo microstimulation[14], as well as silencing[15-17] of feedback can have both facilitating and suppressive effects. However, it is unclear whether the relative retinotopic locations of the feedback source and target relate to the sign of feedback influence.

To map long-range functional connectivity across areas at cellular resolution, we used simultaneous two-photon optogenetics and calcium imaging at the meso-scale (Fig. 1a, top), extending approaches that focused on local connectivity[18]. We co-expressed the calcium indicator GCaMP6s and the soma-targeted excitatory opsin C1V1(t/t)-Kv2.1 in layer 5 IT neurons across V1 and LM (Fig. 1b). We first mapped visual receptive fields and generated retinotopic maps that delineated the border between the two areas (Fig. 1c, & Fig. 2a). We then holographically photostimulated clustered groups of neurons (6-14 targets) and simultaneously recorded population activity at cellular resolution across both cortical areas using two-photon calcium imaging (Fig. 1c, Extended Data Fig. 1a-c). We performed photostimulation simultaneously with visual stimulation, allowing us to resolve small changes in physiological patterns of activity due to our manipulation.

To identify photostimulus-responsive neurons (‘responders’), we compared each neuron’s responses to visual stimulation with and without photostimulation (Fig. 1d) by performing a Wilcoxon rank sum test and controlling for the false discovery rate across all neurons (Methods; Extended Data Fig. 1d & 2a-e). This procedure yielded both facilitated and suppressed neurons in both the directly targeted “local” and the other “across-border” area (Fig. 1e, f; False Discovery Rate = 2.5%, mean number of neurons ± s.d. across stimulation groups locally in V1 54.2 ± 41.2 facilitated, 6.1 ± 17.4 suppressed, local LM: 93.7 ± 52.9, 5.6 ± 10.7; V1 to LM: 0.4 ± 1.2, 1.5 ± 6.3; LM to V1: 1.3 ± 3.3, 1.7 ± 4.8). To reveal the retinotopic distribution of these responders, we computed their retinotopic distance from the photostimulated location, represented by all locally facilitated responders (‘source neurons’; Methods; Fig. 2b). For visualization, we weighted the resulting distribution of retinotopic distances by the distribution of all

neurons in the field of view and averaged across photostimulation groups. This illustrates the over- or under-representation of feedback-facilitated and suppressed neurons across retinotopic distance from the photostimulation site (Fig. 2c,d).

Using this approach, we could examine how local, feedforward (V1 to LM) and feedback (LM to V1) functional connectivity depends on relative topography. Locally, in both V1 and LM, photostimulation caused a spatially restricted facilitation consisting of directly targeted and synaptically recruited neurons (Extended Data Fig. 2). In addition, photostimulation of V1 or LM recruited a local surround of suppression, consistent with recent reports[18] of local functional connectivity in V1 (Fig. 2c). In the feedforward direction, facilitated and suppressed responders were distributed similarly (Fig. 2d, top; Extended Data Fig. 2e). Responders in the feedback direction exhibited a topographic organization: the unweighted locations of facilitated and suppressed responders were significantly displaced relative to each other, with suppressed responders retinotopically closer and facilitated responders farther away from the photostimulated retinotopic location (Fig. 2d, bottom, Extended Data Fig. 2d,e). However, these biases were not absolute: facilitated and suppressed responders overlapped across a wide range of retinotopic distances, where feedback had both positive and negative influence (Fig. 2d). These results did not depend on the false discovery rate (Extended Data Fig. 2d-e), physical distance or differences in stimulation strength between V1 and LM (Extended Data Fig. 3a-e). The number of responders did depend on stimulation strength but the magnitude of response did not vary retinotopically (Extended Data Fig. 3f,g). Finally, individual feedback stimulation groups could generate both facilitated and suppressed across-area responders (Extended Data Fig. 3h). Overall, these results show that the functional influence of feedback from LM to V1 is retinotopically organized, i.e. depends on the retinotopic alignment between source and target. When connections from LM to V1 are between regions responsive to the same portion of visual space (retinotopic distance = 0^o), LM influence over V1 is relatively more suppressive. When connections are between regions responsive to stimuli offset from each other in visual space (retinotopic distance >> 0^o), LM influence over V1 is relatively more facilitating. In other words, feedback influence has a relatively suppressive center and a relatively facilitating surround (Fig. 2e).

Surround stimuli evoke dendritic events

How feedback exerts its influence depends not just on connectivity, but also on synaptic integration by the recipient neurons. While feedback can act through both basal and apical dendritic arbors, integration in apical dendrites is particularly complex: their remoteness from the soma impedes passive integration, but allows them to operate as partially independent compartments that can produce regenerative events associated with calcium entry[7,19,20]. These events could amplify feedback influence[5,19,21,22], as well as perform thresholding and gain control operations[23,24]. It is therefore critical to determine the conditions under which such events are recruited in visual cortex in vivo[25]. Based on the feedback connectivity we observed, we predicted that apical tufts in V1 should receive relatively more facilitating feedback from their retinotopic surround, potentially recruiting regenerative dendritic events to promote their influence on neuronal output.

To test our prediction, we developed a dual recombinase approach for ultra-sparse labelling of layer 5 IT neurons which enabled us to measure calcium signals from fine distal tuft dendrites of individual neurons with minimal contamination from other sources (Fig. 3a). This strategy allowed us to trace fine apical tuft dendrites to their parent somata, map their receptive fields, and finally image the tuft dendrites at high magnification during visual stimulation (Fig. 3b, Extended Data Fig. 4a). To test our prediction, we displayed sinusoidal gratings shaped with Gaussian masks to either cover the center of the receptive field, the surround or various combinations of both, without matching somatic orientation preference (Fig. 3c, Extended Data Fig. 4b).

We found that visual stimuli could evoke local dendritic calcium transients that were spatially more extensive than single spine events, but not as extensive as global calcium events. These involved at least two spines and a limited stretch of the dendritic branch simultaneously activated, while the same branch was not activated proximally (closer to the soma; Fig. 3b, Extended Data Fig. 4c, Supplementary Video 1 and 2). These events were localized in comparison to global events, which involved activation of the entire dendritic branch[25] (Extended Data Video 2). We found 50 such events in 13 branches belonging to 9 neurons, out of a total of 24 branches belonging to 13 neurons imaged. The spatial spread of these local events was variable, but the

average event had a full-width at half maximum of 11.2 μm (Extended Data Fig. 5), similar to the spatial extent of pharmacologically identified NMDA spikes described *in vitro*[7,22,26]. Importantly, the frequency of these events was modulated by visual stimulus type: they occurred most commonly during the presentation of the “inverse” stimulus (Fig. 3c). These results indicate that surround stimuli, which should recruit relatively more facilitating feedback from LM, also recruit NMDA spike-like localized calcium events in tuft dendrites. Functionally, this means that information pertaining to sensory context is locally and nonlinearly integrated in apical dendrites in V1. In comparison, a visual stimulus inside the receptive field produced almost no local events, but did produce global events, which we examined next.

Somatic activity is often associated with global events that engage the entire apical tuft[25]. Such global dendritic events could arise due to backpropagating action potentials (bAPs), dendritic calcium spikes or a combination of both[21,27]. To assess whether global dendritic events carry a similar signature of surround facilitation as do local events, we imaged somata and apical dendrites expressing GCaMP7s semi-sparsely, while presenting Gabor patches of increasing size as visual stimuli, which contain increasingly higher surround energy (Extended Data Figs. 6a,b and 7). Focusing on a population of cells preferring 20° Gabors, we found 53% (n = 30 / 57) of cells individually showed a significant effect of visual stimulus size on dendritic activity after controlling for somatic activity (one-way ANOVA on linear regression residuals, $p < 0.05$; Methods, Extended Data Fig. 6c-e). Residual dendritic signals increased as stimulus size increased to the preferred size. Beyond the preferred size, somata were suppressed, but residual dendritic signals remained elevated on average. Across a larger population of neurons with diverse size preference (n = 131), dendritic residuals were biased to prefer larger visual stimuli than their parent somata (Extended Data Fig. 6f,g). In a second experiment we used the same stimuli as those in Fig. 3 and measured the responses of apical dendrites relative to basal dendrites in individual neurons expressing GCaMP6s ultra-sparsely, finding a similar preference of the apical compartment for stimuli with more surround energy (Extended Data Fig. 8). Thus, visual stimuli with more surround energy recruit the apical dendritic compartment relatively more than the rest of the neuron during global events, similar to the conditions that drove local dendritic events. This increase of apical dendritic recruitment may reflect calcium events of dendritic origin or a modulation of bAP

efficacy. In summary, dendritic events in V1 layer 5 pyramidal cells involving calcium entry with spatial scales ranging from local to global are all modulated by sensory stimuli with a preference for surround stimulation. This suggests that feedback connectivity and dendritic recruitment are co-organized: they obey a similar center-surround organization.

Feedback contributes to dendritic signals

To establish a causal relationship between functional connectivity and dendritic recruitment it is necessary to show that feedback from LM can drive nonlinear dendritic integration in apical dendrites. To test this, we combined two-photon optogenetic stimulation of LM neurons with simultaneous apical dendritic imaging in V1 in two sets of experiments (Fig. 4a) where we expressed soma-restricted C1V1 in LM, and GCaMP6s ultra-sparsely in V1. First, stimulating clustered groups of LM neurons (25 targets per cluster) while imaging apical dendritic segments in V1 (Fig. 4b, c) reduced the average calcium signals measured from apical dendrites (Fig. 4d). Random 20% subsamples of all stimulation group-dendrite pairs consistently yielded suppression of calcium signals, with only 0.7% of subsamples producing an average response above zero. This suggests that feedback suppression mediated by LM is dense and non-specific, while feedback facilitation may be sparse.

Next, to identify potentially rare facilitating connections and stimulate them in isolation, we sought to increase the number of potential connections we assayed in a single experiment. To this end we stimulated random groups of 8 - 25 targets drawn from a 3D target grid in LM composed of thousands of targets, and recorded the responses of all visible spines on apical dendrites we imaged in V1 (Fig. 4e, f). In these experiments, opsin expression was either limited to TLX+ neurons, or also included layer 2/3 to increase the number of potential presynaptic partners. Using online analysis of stimulation-triggered spine signals we identified potentially connected pairs of optogenetic targets and responsive spines (Extended Data Fig. 9a-c). We then performed targeted stimulation of the putative presynaptic neurons either individually or in small groups to validate individual connections (Fig. 4g). Remarkably – given the considerable distance between targets in LM and the recipient neurons in V1, as well as the challenge of finding the relevant spines on the postsynaptic pyramidal cell being

imaged – we were able to confirm a substantial number of spines as unambiguously responsive to stimulation of individual targets in LM (Fig. 4h, Extended Data Fig. 9d-g signed rank test, pre-stim vs post-stim, $p < 0.01$; 34 significantly responsive spines in 26 neurons in 11 animals out of 147 recordings in 25 animals). Detection of spines active in isolation (Supplementary Video 3) confirmed that the signals were driven by synaptic input from LM. These results directly identify the presynaptic source and postsynaptic targets of LM inputs on the apical dendrites of layer 5 pyramidal cells in V1, and indicate that feedback excitation mediated by LM is sparse.

Having identified excitatory connections between LM neurons and V1 apical dendrites, we next asked if this excitatory feedback can recruit local dendritic calcium signals. Strikingly, in the apical tuft of some V1 layer 5 pyramidal neurons, LM stimulation triggered local dendritic calcium events which resembled the visually-evoked local events shown in Figure 3 (4 out of 26 neurons, on one to five trials per neuron; Fig. 4i,j; Extended Data Fig. 10 a,b, Supplementary Video 4). This suggests that feedback input from LM is capable of triggering local dendritic nonlinear events in the apical tuft of V1 pyramidal neurons. Next, to provide further support for recruitment of dendritic nonlinearities by feedback, we examined whether LM inputs can boost calcium signals in the recipient dendritic branch. We identified a spine activated by LM input, and quantified the photostimulation-induced modulation of neighbouring dendritic calcium signals in that branch in comparison to calcium signals recorded from a sister branch (Fig. 4k-n). We placed a “target” ROI distally on the branch containing the feedback-recipient spine, but excluding the spine itself (mean minimum spine-to-ROI distance across cells: 5 µm, Fig. 4l). We placed another, “reference” ROI for comparison on a different branch belonging to the same neuron, or occasionally more proximally on the same branch (ROIs identified for 25/34 spines) and calculated the ratio of calcium signals from the stimulated branch versus that of the reference (the “boosting index”, Fig. 4m,n). We compared the boosting index computed for feedback photostimulation trials to blank trials lacking photostimulation (Fig. 4o). We found that photostimulation of LM inputs preferentially enhanced calcium signals in the branch containing the activated spine relative to the reference branch (increase in boosting index 10.8 ± 2.2%, mean ± s.e.m.; $p = 0.0002$, Fig. 4o). Repeating this analysis with the target ROI moved further away from the feedback recipient spine (minimum spine-to-ROI distance 10.5 ± 1.05 µm, mean ± s.e.m.) produced the same result, conservatively

showing that this effect is spatially extended beyond the spine itself (Extended Data Fig. 10c, d). This effect did not depend on retinotopic distance and was present regardless of whether feedback photostimulation was performed simultaneously with visual stimulation or on its own (Extended Data Fig. 10e-h). Thus, we provide causal evidence that LM input can trigger local dendritic calcium signals similar to those driven by surround visual stimuli, and can also drive branch-specific boosting of ongoing spontaneous and visually evoked activity.

Taken together, these results reveal several previously unknown features of feedback. First, feedback suppression is dense, arising from many LM neurons. Second, feedback facilitation is sparse, arising from few LM neurons. Third, feedback can drive branch-specific local calcium signals that are spatially extended beyond individual feedback recipient spines. Lastly, feedback-driven calcium signals can be large enough to account for local dendritic calcium events driven by visual stimuli. Overall, these results establish a causal connection between LM feedback and apical dendritic calcium signals reflecting nonlinear postsynaptic integration.

Behavior regulates feedback and dendrites

If feedback and dendritic recruitment are causally related, they may also be co-regulated by learning[28,29], behavior[3,6] or on shorter timescales by moment-to-moment variations in behavioral state[25]. To ask whether behavioral state regulates feedback and dendrites we focused on locomotion[30,31] and found that it enhances visual responses in L5 of LM (Extended Data Fig. 11a,b), similar to findings in layer 2/3 of LM[32]. Predicting that increased activity in LM might lead to increased feedback facilitation as well as inhibition of apical dendrites in V1, we measured glutamate and GABA signals in layer 1 of V1 using the genetically encoded sensors iGluSnFR-A184S (Methods, Extended Data Fig. 12) and iGABA-SnFR (Methods, Extended Data Fig. 13), and found that locomotion enhanced both signals. Given the increased activity in LM and increased input to apical dendrites associated with locomotion, we next looked for changes in dendritic calcium signals in V1. We found that apical dendritic activity was suppressed by locomotion during the presentation of visual stimuli smaller than the neurons' preferred size, while it did not change for larger stimuli (Extended Data Fig. 11d-f). Locomotion also reduced somatic responses to small stimuli, while

enhancing responses to larger visual stimuli (as seen previously[31]; Extended Data Fig. 11g-i). Reduction of somatic and dendritic responses to small stimuli is consistent with increased feedback suppression of apical dendrites. However, the locomotion-induced somatic enhancement in response to larger stimuli is incompatible with the lack of apical dendritic enhancement for larger stimulus sizes and must instead be mediated by basal dendrites. To resolve this we performed a dual-color two-photon input-output imaging experiment, measuring basal and apical glutamatergic inputs and output activity using the red calcium indicator jRGECO1a (Methods, Extended Data Fig. 11j and 12). A linear fit to the relationship of dendritic inputs to population output indicated that during locomotion, apical inputs become less effective while basal inputs become more effective, potentially supporting the enhancement of responses to larger stimuli (Extended Data Fig. 11k, l and 12l-n). This enhancement may involve changes in basal dendritic excitability[26] as well as enhanced thalamic responses[33], and an NDNF-interneuron mediated shift of inhibition from the soma to apical dendrites[34]. Collectively, these results are consistent with our framework of feedback modulation of dendritic excitability. In summary, while locomotion involves diverse and distributed changes throughout the brain, our results suggest that moment-to-moment changes in dendritic excitability linked to modulation of feedback may be a contributing mechanism.

Discussion

Our experiments reveal novel findings about the organization of cortical feedback, nonlinear dendritic integration, and their relationship in vivo. First, we developed a powerful new all-optical strategy for probing functional connectivity between brain areas at cellular resolution, which revealed a novel retinotopic organization of feedback in visual cortex: LM is relatively more suppressive of V1 when connections are between regions responsive to the same part of visual space. Conversely, LM is relatively more facilitating of V1 when connections are between regions responsive to more distant parts of visual space. This “suppressive-center, facilitating-surround” organization contrasts with feedback from frontal cortex: projections from cingulate cortex exhibit a facilitating center and suppressive surround in V1[35]. This difference may reflect distinct functions of feedback from different sources: while feedback from frontal cortex may support attentional modulation[35], our results are more consistent with models of predictive coding[36,37]. Feedback from higher visual areas has been modelled using subtractive elements carrying predictions[38]. We provide mechanistic support for such models by validating one of their tenets: feedback aligned to the feedforward hierarchy should be suppressive[36] (consistent with silencing experiments[15,16] and cortico-thalamic feedback[39]). Identifying the inhibitory circuits that mediate feedback suppression will be crucial. Our demonstration of a “facilitating surround” in turn provides a circuit mechanism for cooperative interactions between stimuli and their sensory context[40,41] as well as for excitatory responses to surround-only visual stimuli[17,42]. Silencing LM reduces V1 responses to surround-only visual stimuli[17], which is consistent with our results on LM to V1 functional connectivity, and our demonstration that LM inputs can engage dendritic nonlinearities in V1. The generality of these results may be constrained by technical factors such as the limited temporal resolution of GCaMP, which may obscure faster modulations of feedback[43]. Similarly, functional connectivity may depend on visual contrast, feature selectivity, cell types, cortical layer and source area. It will be crucial to understand these dependencies and identify the synaptic wiring diagram that underlies functional connectivity.

To understand how feedback works it is essential to reveal how it is implemented on the cellular level. By combining targeted stimulation of neurons in LM with high-resolution imaging of dendritic arbors in V1, we provide the first demonstration of

independent local dendritic events selectively recruited by sensory stimuli designed to enhance feedback. We then identify feedback recipient spines and show directly that stimulation of feedback inputs to these spines can both drive and enhance branch-specific dendritic calcium signals extending beyond the identified spines. These findings suggest that feedback from LM contributes to the generation of active dendritic events in response to visual stimuli. It will be important to determine whether LM inputs or any other specific inputs are necessary for the recruitment of active dendritic events, and whether natural patterns of feedback activity recruit them. It will also be important to confirm the underlying voltage profile, true frequency and biophysical basis of these events, which are consistent with NMDA spikes[22,26] but could also involve other mechanisms, such as other types of dendritic spikes[5,20,21] or intracellular calcium release[44].

Active dendritic integration has been shown to contribute to feature selectivity[45-47]. Here we show that sensory context (visual surround) also engages nonlinear dendritic mechanisms within apical tuft dendrites. By showing that feedback inputs can trigger local events in individual dendritic branches, and can also produce branch-specific boosting of dendritic activity, our study provides crucial support for the longstanding proposal that branch-specific computations are exploited in vivo[19,23,26]. Describing dendritic recruitment rules under natural behavioral and sensory conditions will be critical to a mechanistic understanding of how feedback contributes to cortical computations like contour integration and figure-ground segmentation[3]. Feedback may generate somatic responses directly[17] by driving active dendritic events, or it could indirectly affect dendritic integration, as engaging dendritic nonlinearities can change input-output gain both locally[48] and globally[24] to make other inputs, such as long range horizontal inputs[11,49], more effective. Such gain-control may allow contour integration to rely on the cooperative interaction of feedback and horizontal excitatory connections[50]. Since basal dendrites also receive feedback[4], it will be important to understand how their excitability may also be involved in mediating feedback influence.

Finally, we find that active behavioral states are associated with increased activity in a prominent feedback source to V1, increased input onto apical dendrites and modulation of dendritic calcium signals in a manner consistent with feedback

topography. Our results suggest a model where coordinated regulation of feedback and apical dendritic excitability contributes to sculpting visual representations. Since inter-areal feedback projections and active dendritic integration are both ubiquitous features of neocortex, the fact that they are systematically related suggests that these mechanisms may represent general principles governing coordination among cortical areas.

Acknowledgements

We thank Selmaan Chettih and Chris Harvey for providing C1V1-Kir2.1 virus; Karl Deisseroth for providing fDIO-GCaMP6s virus; Jonathan Marvin and Loren Looger for providing SnFR viruses; Brendan Bicknell, Matteo Carandini, Beverley Clark, James Jeanne, Brendan Lehnert, Federico Rossi, Arnd Roth, William Tobin, and members of the Neural Computation Laboratory for helpful discussions and comments on the manuscript; Soyon Chun, Agnieszka Jucht and Olivia Houghton for mouse breeding and Bruker Corporation for technical support. This work was supported by the Wellcome Trust (M.H., PRF 201225 and 224668), ERC (M.H., AdG 695709, M.F., MSCA-IF 661132), and EMBO (M.F., ALTF 1330-2014).

Author contributions

M.F., D.H. and M.H. conceived the project and wrote the manuscript. D.H. performed experiments involving all-optical interrogation during population imaging. M.F. and D.H. performed ultra-sparse dendritic imaging experiments. M.F. and D.H. performed experiments involving all-optical stimulation during dendritic imaging. M.F., D.H., M.C. and L.B. contributed to performing dendritic volume imaging experiments. M.F., D.H., A.E.W., M.C., and L.B. contributed to dual color imaging experiments. T.-Y.L. contributed to technique development. L.R. wrote software and contributed to technique development. M.F. and D.H. performed all analyses.

References

1 Van Essen, D. C. & Maunsell, J. H. R. Hierarchical Organization and Functional Streams in the Visual-Cortex. *Trends in Neurosciences* **6**, 370-375, doi:Doi 10.1016/0166-2236(83)90167-4 (1983).

2 Gilbert, C. D. & Li, W. Top-down influences on visual processing. *Nat Rev Neurosci* **14**, 350-363, doi:10.1038/nrn3476 (2013).

3 Lamme, V. A. & Roelfsema, P. R. The distinct modes of vision offered by feedforward and recurrent processing. *Trends Neurosci* **23**, 571-579, doi:10.1016/s0166-2236(00)01657-x (2000).

4 Harris, J. A. *et al.* Hierarchical organization of cortical and thalamic connectivity. *Nature* **575**, 195-202, doi:10.1038/s41586-019-1716-z (2019).

5 Williams, S. R. & Stuart, G. J. Dependence of EPSP efficacy on synapse location in neocortical pyramidal neurons. *Science* **295**, 1907-1910, doi:10.1126/science.1067903 (2002).

6 Xu, N. L. *et al.* Nonlinear dendritic integration of sensory and motor input during an active sensing task. *Nature* **492**, 247-251, doi:10.1038/nature11601 (2012).

7 Major, G., Larkum, M. E. & Schiller, J. Active properties of neocortical pyramidal neuron dendrites. *Annu Rev Neurosci* **36**, 1-24, doi:10.1146/annurev-neuro-062111-150343 (2013).

8 Wang, Q. & Burkhalter, A. Area map of mouse visual cortex. *J Comp Neurol* **502**, 339-357, doi:10.1002/cne.21286 (2007).

9 Kim, E. J., Juavinett, A. L., Kyubwa, E. M., Jacobs, M. W. & Callaway, E. M. Three Types of Cortical Layer 5 Neurons That Differ in Brain-wide Connectivity and Function. *Neuron* **88**, 1253-1267, doi:10.1016/j.neuron.2015.11.002 (2015).

10 Takahashi, N. *et al.* Active dendritic currents gate descending cortical outputs in perception. *Nat Neurosci*, doi:10.1038/s41593-020-0677-8 (2020).

11 Angelucci, A. *et al.* Circuits for local and global signal integration in primary visual cortex. *J Neurosci* **22**, 8633-8646 (2002).

12 Marques, T., Nguyen, J., Fioreze, G. & Petreanu, L. The functional organization of cortical feedback inputs to primary visual cortex. *Nat Neurosci* **21**, 757-764, doi:10.1038/s41593-018-0135-z (2018).

13 Shen, S. *et al.* Distinct organization of two cortico-cortical feedback pathways. *Nat Commun* **13**, 6389, doi:10.1038/s41467-022-33883-9 (2022).

14 Klink, P. C., Dagnino, B., Gariel-Mathis, M. A. & Roelfsema, P. R. Distinct Feedforward and Feedback Effects of Microstimulation in Visual Cortex Reveal Neural Mechanisms of Texture Segregation. *Neuron* **95**, 209-220 e203, doi:10.1016/j.neuron.2017.05.033 (2017).

15 Nassi, J. J., Lomber, S. G. & Born, R. T. Corticocortical feedback contributes to surround suppression in V1 of the alert primate. *J Neurosci* **33**, 8504-8517, doi:10.1523/JNEUROSCI.5124-12.2013 (2013).

16 Nurminen, L., Merlin, S., Bijanzadeh, M., Federer, F. & Angelucci, A. Top-down feedback controls spatial summation and response amplitude in primate visual cortex. *Nat Commun* **9**, 2281, doi:10.1038/s41467-018-04500-5 (2018).

17 Keller, A. J., Roth, M. M. & Scanziani, M. Feedback generates a second receptive field in neurons of the visual cortex. *Nature*, doi:10.1038/s41586-020-2319-4 (2020).

18 Chettih, S. N. & Harvey, C. D. Single-neuron perturbations reveal feature-specific competition in V1. *Nature* **567**, 334-340, doi:10.1038/s41586-019-0997-6 (2019).

19 Larkum, M. E., Nevian, T., Sandler, M., Polsky, A. & Schiller, J. Synaptic integration in tuft dendrites of layer 5 pyramidal neurons: a new unifying principle. *Science* **325**, 756-760, doi:10.1126/science.1171958 (2009).

20 Schiller, J., Schiller, Y., Stuart, G. & Sakmann, B. Calcium action potentials restricted to distal apical dendrites of rat neocortical pyramidal neurons. *J Physiol* **505 (Pt 3)**, 605-616, doi:10.1111/j.1469-7793.1997.605ba.x (1997).

21 Larkum, M. E., Zhu, J. J. & Sakmann, B. A new cellular mechanism for coupling inputs arriving at different cortical layers. *Nature* **398**, 338-341, doi:10.1038/18686 (1999).

22 Palmer, L. M. *et al.* NMDA spikes enhance action potential generation during sensory input. *Nat Neurosci* **17**, 383-390, doi:10.1038/nn.3646 (2014).

23 Poirazi, P., Brannon, T. & Mel, B. W. Pyramidal neuron as two-layer neural network. *Neuron* **37**, 989-999, doi:10.1016/s0896-6273(03)00149-1 (2003).

24 Larkum, M. E., Senn, W. & Luscher, H. R. Top-down dendritic input increases the gain of layer 5 pyramidal neurons. *Cereb Cortex* **14**, 1059-1070, doi:10.1093/cercor/bhh065 (2004).

25 Francioni, V., Padamsey, Z. & Rochefort, N. L. High and asymmetric somato-dendritic coupling of V1 layer 5 neurons independent of visual stimulation and locomotion. *Elife* **8**, doi:10.7554/eLife.49145 (2019).

26 Schiller, J., Major, G., Koester, H. J. & Schiller, Y. NMDA spikes in basal dendrites of cortical pyramidal neurons. *Nature* **404**, 285-289, doi:10.1038/35005094 (2000).

27 Larkum, M. E., Kaiser, K. M. & Sakmann, B. Calcium electrogenesis in distal apical dendrites of layer 5 pyramidal cells at a critical frequency of back-propagating action potentials. *Proc Natl Acad Sci U S A* **96**, 14600-14604, doi:10.1073/pnas.96.25.14600 (1999).

28 Roelfsema, P. R. & Holtmaat, A. Control of synaptic plasticity in deep cortical networks. *Nat Rev Neurosci* **19**, 166-180, doi:10.1038/nrn.2018.6 (2018).

29 Cichon, J. & Gan, W. B. Branch-specific dendritic Ca(2+) spikes cause persistent synaptic plasticity. *Nature* **520**, 180-185, doi:10.1038/nature14251 (2015).

30 Niell, C. M. & Stryker, M. P. Modulation of visual responses by behavioral state in mouse visual cortex. *Neuron* **65**, 472-479, doi:10.1016/j.neuron.2010.01.033 (2010).

31 Ayaz, A., Saleem, A. B., Scholvinck, M. L. & Carandini, M. Locomotion controls spatial integration in mouse visual cortex. *Curr Biol* **23**, 890-894, doi:10.1016/j.cub.2013.04.012 (2013).

32 Lecoq, J. *et al.* Visualizing mammalian brain area interactions by dual-axis two-photon calcium imaging. *Nat Neurosci* **17**, 1825-1829, doi:10.1038/nn.3867 (2014).

33 Erisken, S. *et al.* Effects of locomotion extend throughout the mouse early visual system. *Curr Biol* **24**, 2899-2907, doi:10.1016/j.cub.2014.10.045 (2014).

34 Cohen-Kashi Malina, K. *et al.* NDNF interneurons in layer 1 gain-modulate whole cortical columns according to an animal's behavioral state. *Neuron* **109**, 2150-2164 e2155, doi:10.1016/j.neuron.2021.05.001 (2021).

35 Zhang, S. *et al.* Selective attention. Long-range and local circuits for top-down modulation of visual cortex processing. *Science* **345**, 660-665, doi:10.1126/science.1254126 (2014).

36 Bastos, A. M. *et al.* Canonical microcircuits for predictive coding. *Neuron* **76**, 695-711, doi:10.1016/j.neuron.2012.10.038 (2012).

37 Keller, G. B. & Mrsic-Flogel, T. D. Predictive Processing: A Canonical Cortical Computation. *Neuron* **100**, 424-435, doi:10.1016/j.neuron.2018.10.003 (2018).

38 Rao, R. P. & Ballard, D. H. Predictive coding in the visual cortex: a functional interpretation of some extra-classical receptive-field effects. *Nat Neurosci* **2**, 79-87, doi:10.1038/4580 (1999).

39 Wang, W., Jones, H. E., Andolina, I. M., Salt, T. E. & Sillito, A. M. Functional alignment of feedback effects from visual cortex to thalamus. *Nat Neurosci* **9**, 1330-1336, doi:10.1038/nn1768 (2006).

40 Kapadia, M. K., Ito, M., Gilbert, C. D. & Westheimer, G. Improvement in visual sensitivity by changes in local context: parallel studies in human observers and in V1 of alert monkeys. *Neuron* **15**, 843-856, doi:10.1016/0896-6273(95)90175-2 (1995).

41 Sillito, A. M., Grieve, K. L., Jones, H. E., Cudeiro, J. & Davis, J. Visual cortical mechanisms detecting focal orientation discontinuities. *Nature* **378**, 492-496, doi:10.1038/378492a0 (1995).

42 Self, M. W. *et al.* Orientation-tuned surround suppression in mouse visual cortex. *J Neurosci* **34**, 9290-9304, doi:10.1523/JNEUROSCI.5051-13.2014 (2014).

43 Javadzadeh, M. & Hofer, S. B. Dynamic causal communication channels between neocortical areas. *bioRxiv*, doi:10.1101/2021.06.28.449892 (2021).

44 O'Hare, J. K. *et al.* Compartment-specific tuning of dendritic feature selectivity by intracellular Ca(2+) release. *Science* **375**, eabm1670, doi:10.1126/science.abm1670 (2022).

45 Smith, S. L., Smith, I. T., Branco, T. & Hausser, M. Dendritic spikes enhance stimulus selectivity in cortical neurons in vivo. *Nature* **503**, 115-120, doi:10.1038/nature12600 (2013).

46 Lavzin, M., Rapoport, S., Polsky, A., Garion, L. & Schiller, J. Nonlinear dendritic processing determines angular tuning of barrel cortex neurons in vivo. *Nature* **490**, 397-401, doi:10.1038/nature11451 (2012).

47 Wilson, D. E., Whitney, D. E., Scholl, B. & Fitzpatrick, D. Orientation selectivity and the functional clustering of synaptic inputs in primary visual cortex. *Nat Neurosci* **19**, 1003-1009, doi:10.1038/nn.4323 (2016).

48 Branco, T. & Hausser, M. Synaptic integration gradients in single cortical pyramidal cell dendrites. *Neuron* **69**, 885-892, doi:10.1016/j.neuron.2011.02.006 (2011).

49 Iacaruso, M. F., Gasler, I. T. & Hofer, S. B. Synaptic organization of visual space in primary visual cortex. *Nature* **547**, 449-452, doi:10.1038/nature23019 (2017).

50 Liang, H. *et al.* Interactions between feedback and lateral connections in the primary visual cortex. *Proc Natl Acad Sci U S A* **114**, 8637-8642, doi:10.1073/pnas.1706183114 (2017).

Fig. 1 | Mesoscale mapping of inter-areal functional connectivity in mouse visual cortex using simultaneous two-photon optogenetic stimulation and two-photon calcium imaging.

a, Top, illustration of experimental setup to probe inter-areal functional connectivity between primary visual cortex (V1) and the lateral-medial higher visual area LM. Bottom, schematic of pyramidal neurons with layer-specific projection preferences.

b, Mean two-photon images for one example field-of-view showing large spatial extent of expression. Top, GCaMP6s expression driven transgenically, and bottom, C1V1 expression, driven using AAVs. Insets show representative cell bodies.

c, Top, cellular resolution retinotopic maps for a large field-of-view, obtained using sparse noise stimulation and two-photon population imaging. Gray bar delineates 150 μm wide border zone, which was excluded from stimulation and responder detection. Bottom, mean photostimulation response of example stimulation groups (pixelwise stimulus-triggered averages).

d, Trial structure. Full field sinusoidal gratings were presented either alone, or paired with a photostimulus. Responses to the two trial types were compared to detect “responders”.

e, Example local responders from one session (mean ± s.e.m. across trials). Bar represents visual stimulus presentation. Both examples from LM.

f, Example across-border (in the area opposite the stimulated one) responders from one session. Facilitated example from LM, suppressed from V1.

Fig. 2 | Cortico-cortical feedback is relatively suppressive of topographically matched “center” locations and relatively facilitating of mismatched “surround” locations.

a, Left, retinotopic map in azimuth used to assign recorded neurons to a cortical area was obtained by smoothing cellular resolution maps constructed using sparse noise stimuli and two-photon population imaging. Right, smoothed retinotopic map in elevation.

b, Left, example photostimulation group in LM (probing functional connectivity in the feedback direction) and corresponding retinotopic location in V1. Right, measurement of absolute retinotopic (rather than physical) distance of an example across-border responder to photostimulated cluster.

c, Probability distribution of responder retinotopic distances divided by the probability distribution of distances for all available neurons (mean ± s.e.m. across stimulation groups, n = 129 LM and n = 180 V1 clusters from 42 sessions in 11 animals). Horizontal gray lines mark y = 1 and represent uniform spatial sampling. Suppressed responders are plotted downward by convention. Red arrow indicates location of stimulation, green arrow indicates location of responders measured. Top, stimulation and readout in V1. Bottom, stimulation and readout in LM.

d, Same as c, for inter-areal stimulation and readout but also including the average retinotopic location of responders for each stimulation group (red and blue dots), which are used to make the comparison. Top, stimulation in V1 and readout in LM (feedforward). Bottom, stimulation in LM and readout in V1 (feedback). Feedforward facilitated and suppressed responders do not differ in spatial distribution (centroids over stimulation groups, rank-sum, $p = 0.61$). Feedback facilitated and suppressed responders are displaced relative to each other (rank-sum, $p = 9.2 \times 10^{-5}$).
e, Schematic illustrating the suppressive feedback from retinotopically aligned and facilitating feedback from retinotopically offset projections.

Fig. 3 | Visual stimuli that recruit facilitating feedback drive local calcium events in apical tuft dendrites.
a, Experimental design. Ultra-sparse expression within layer 5 IT neurons defined by Cre-expression was achieved by combining AAV mediated Cre-dependent FLP expression with AAV-mediated FLP-dependent GCaMP6s expression. Isolated somata were identified with two-photon imaging, their receptive fields mapped, and apical dendrites traced. Visual stimuli were then positioned relative to the receptive field and visual responses of the identified dendrites imaged.
b, Example local dendritic events from two different neurons. Top left, mean dendritic segment fluorescence during global events, middle left, mean fluorescence during local dendritic event, bottom left, local dendritic event magnified: note at least two spines are simultaneously active along with a limited extent of the adjacent branch. Top, right, manually drawn ROIs, and illustration of their location on an idealized pyramidal cell morphology. Inset, blow-up of independent event. Following example as in the first.
c, Stimulus-dependence of independent events showing that the inverse stimulus, which provides the most effective stimulation of the surround, drives the most independent events. Results from n = 13 branches belonging to 9 neurons. Lines connect responses obtained from a single branch (17 trials per minute). Kruskal-Wallis test across all stimuli, $p = 0.01$, followed by post-hoc Dunn's: 8^o vs inverse: $p = 0.041$,16^o vs inverse: $p = 0.047$, inverse vs annulus: $p = 0.034$, inverse vs full-field: $p = 0.48$. Stimuli are schematized as disks to illustrate size and shape, presented experimentally as sinusoidal gratings with Gaussian masks and no sharp edges.
d, Schematic illustrating topographically offset feedback facilitating events in apical tuft dendrites.

Fig. 4 | LM feedback drives branch-specific local dendritic calcium signals in V1.

a, Two-photon optogenetic stimulation of LM neurons during simultaneous two-photon imaging of apical dendrites in V1.

b, Left, opsin expression and target groups in LM for clustered stimulation. Right, sparse GCaMP expression in V1.

c, Top, example dendrite. Bottom, fluorescence from blue ROI, photostimulation in red.

d, Average photostimulation response in blue, average blank trial in black (n = 71 dendrites in 14 animals, signed rank tests, pre vs post stim $p = 1.1 \times 10^{-7}$, pre vs post blank $p = 0.74$, stim vs blank $p = 3.2 \times 10^{-6}$).

e, Grid of targets for random stimulation, one group in yellow.

f, Top, example dendrite and spine ROIs. Bottom, fluorescence from three ROIs. Arrowhead indicates independent spine event.

g, Testing a putative connection (target #1095 → spine #1) after it was identified through analysis of independent events.

h, Isolated stimulation confirms connection. Top, photostimulus-triggered average image showing responsive spine. Bottom, blank and photostimulus responses from spine.

i, Two examples of photostimuluation-triggered local events. Left, global event showing stimulated and reference branch ROIs. Middle, responsive spines. Right, single trial showing branch-specific event.

j, Fluorescence from ROIs in (i).

k, Example FOV for boosting analysis showing ROI on reference branch and box around branch carrying a feedback recipient spine.

l, Top, higher magnification image showing feedback recipient spine (arrowhead) and ROI excluding it. Bottom, ideal layout of ROIs for boosting analysis.

m, Top, example photostimulation trial showing fluorescence from the synaptically stimulated branch and reference branch. Bottom, same for blank trial.

n, Distributions of boosting indices for stimulation and blank trials from one recording with significant boosting (rank-sum, $p = 1.16 \times 10^{-8}$). Dashed lines indicate means.

o, Mean boosting indices for photostimulation trials are higher than for blank trials across recordings (paired t-test, $p = 0.0002$). Filled circles are individually significantly modulated neurons ($p < 0.05$).

Methods

All experimental procedures were carried out under license from the UK Home Office in accordance with the UK Animals (Scientific Procedures) Act (1986).

Mice and surgeries. Male and female TLX3-Cre or TLX3-Cre; CaMKII-tTA; TITL-GCaMP6s mice aged between seven and ten weeks were used. TLX3-Cre (PL56) is a GENSAT BAC transgenic and has been previously described[9,51]. The other two parental lines were obtained from The Jackson Laboratories (CaMKII-tTA, # 007004, Ref. [52] and TITL-GCaMP6s (Ai94,) #024104, Ref. [53]). Four to eight hours before surgery, mice were given an injection of dexamethasone (Dexadreson, 5 mg/kg body weight at 2 mg/ml; Ref. [54]). Immediately before surgery, mice were given a subcutaneous injection of buprenorphine hydrochloride (Vetergesic, 1 mg/kg body weight at 0.3 mg/mL) and anesthetized with isoflurane (5% induction, <1.5% maintenance). The scalp was removed and an aluminum or titanium headplate with an 11 mm circular opening was fixed to the skull with dental cement (Super-Bond C&B, Sun-Medical). A craniotomy was performed over caudal-lateral cortex and the dura carefully removed. A calibrated pipette (Drummond Scientific Company, Wiretrol II Cat. 5-000-2005) bevelled to a sharp point and connected to a hydraulic injection system (Narishige MO-1) was used to inject virus, which was diluted in a buffer solution (20 mM Tris, 140 mM NaCl, 0.001% Pluronic F-68, pH 8.0). Virus injections were made 500 µm below the surface at 0.1 µL/min. Injection locations were determined using stereotactic coordinates and blood vessel patterns. Subsequent retinotopic mapping was used to confirm intended coverage of the visual cortex. After each injection, the pipette was maintained in position for 5 minutes before retraction. Chronic imaging windows were constructed using a single 4 mm coverslip with small pieces of coverslip optically glued to the top side to serve as added surface to support dental cement. Craniotomies were sealed with cyanoacrylate glue (Vetbond, 3M) and windows fixed in place with dental cement. Animals were allowed to recover for at least 5 days. Subsequently, animals were acclimatized to the microscopes and styrofoam running wheels for 2-5 sessions before experiments. The number of mice included in each experiment is as follows: two-photon stimulation and population imaging (Figs. 1-2): 15; two-photon stimulation and dendritic imaging: 14 for Fig. 4a-d, 10 for Fig. 4e-o; ultra-sparse dendritic imaging (Fig. 3): 5 animals; ultra-sparse dendritic volume

imaging (Extended Data Fig. 8): 10; semi-sparse dendritic imaging (Extended Data Figs. 6,7,11): 9; dual-color glutamate imaging: 4; dual-color GABA imaging: 7.

Two-photon optogenetic stimulation and population imaging. Simultaneous all-optical interrogation across LM and V1 circuits was carried out by adapting existing approaches[55-62] using a large field-of-view resonant scanning microscope (Ultima 2P plus, Bruker). Expression of calcium indicator and opsin was achieved by injecting AAV2/9-*Ef1a*-DIO-C1V1(t/t)-mRuby2-Kv2.1 (Selmaan Chettih, Christopher Harvey; Harvard Medical School) diluted 1:13 from a stock concentration of ~6.9 x 10^{14} gc/ml into TLX3-Cre;CaMKII-tTA;TITL-GCaMP6s animals. 200 nL of virus was injected into a grid of six locations positioned ~300 µm apart over LM and V1 guided by the blood vessel patterns. Two-photon calcium imaging was performed using 920 nm light delivered from a tunable laser (InSight X3, Spectra-Physics). Simultaneous two-photon optogenetic excitation was performed using 1030 nm light delivered from a fixed wavelength fiber laser at 1 MHz repetition rate (Satsuma HP2, Amplitude Systèmes). Objectives used were a 16x/0.8NA (Nikon, 32/42 sessions in 11 animals) or a 10x/0.5NA (Thor, TL10X-2P, 10/42 sessions in 4 animals), yielding field-of-view sizes of 1215 or 1920 µm respectively. Volumetric calcium imaging data were acquired using an electrically tuneable lens (Optotune) focusing four planes spaced by 30 µm (7 Hz, 16x) or two planes spaced by 50 µm (15 Hz, 10x). Power post-objective was between 50-100 mW depending on expression level and imaging depth, which was 350-450 µm below the pia. Two-photon optogenetic stimulation was performed using a programmable reflective spatial light modulator (SLM) installed in-line with the stimulation path[56,57,59,63]. The 16x/0.8 NA objective was paired with an SLM (Boulder Nonlinear Systems) with 512 x 512 pixels and 7.68 x 7.68 mm active area, while the 10x / 0.5NA objective was paired with an SLM (Meadowlark Optics) with 1920 x 1152 pixels and 17.6 x 10.7 mm active area. Phase masks were computed via the weighted Gerchberg-Saxton algorithm and loaded using Blink (Meadowlark). The SLM was calibrated to compensate the decrease in diffraction efficiency for peripheral targets, and power per neuron kept constant at 12 mW. Imaging space to SLM space conversion was achieved by burning 3D patterns into plastic slides, taking volumetric stacks, measuring burn locations and fitting affine transformations. To increase stimulation efficiency, the center of the SLM space was offset using galvanometers such that it was close to the centroid of the current stimulation targets. Calibrations

were performed using custom software written in MATLAB[64] (https://github.com/llerussell/SLMTransformMaker3D). Stimulation patterns consisted of multiple beamlets targeting between 6 and 14 neurons. Beamlets were scanned using galvanometers moving in spiral scan patterns (10 repeats of ~16 µm, 20 ms spiral scans at 20 Hz). Synchronization was performed as previously described[64]. Fields-of-view (FOVs) over V1 and LM were determined using retinotopic maps obtained from preparatory widefield and two-photon retinotopic mapping sessions (see below). For stimulation experiments, FOVs were relocated using blood vessel patterns and the data were affine transformed to register the field to previously obtained retinotopic maps. At the beginning of the experiment, neurons responsive to photostimulation were detected using the Near Automatic Photoactivation Response Mapping (NAPARM, https://github.com/llerussell/Naparm) protocol described previously[62,64]. Stimulation clusters were then designed by randomly choosing seed neurons and finding their nearest neighbours from all photoresponsive neurons. A 200 µm wide V1/LM border zone and the top 50 lines of the two-photon frames were excluded from consideration as targets. In each experiment between 5 and 10 (8 ± 1.1) target clusters were stimulated for a total of 129 clusters in LM and 180 clusters in V1 in 42 sessions, 15 animals. Experiments contained 1337 ± 142 trials (mean ± s.d.). Of these trials, 20% (in 40/42 experiments) or 50% (in 2/42 experiments) contained only visual stimulation composed of a two second stimulus and six second inter-trial interval (V trials). The remaining trials contained the same visual stimulus and a two-photon photostimulus (duration 500 ms, triggered 500 ms after visual stimulus onset) of a single target cluster (V+P trials). Each cluster was stimulated in 52 to 175 (mean = 133.4 ± 25) trials.

Ultra-sparse dendritic imaging: Ultra-sparse expression of calcium indicator within a Cre recombinase expressing population of pyramidal neurons was achieved using the virus mixture: AAV2/1-*Ef1a*-DIO-FLPo (gift of Li Zhang, Addgene viral prep #87306-AAV1) diluted 1:75,000 to 1:100,000 from stock concentration of 1.4 x 10^{13} gc/ml and AAVDJ-*Ef1a*-fDIO-GCaMP6s (gift of Karl Deisseroth, Stanford AAV-165) diluted 1:9 from stock concentration of 7.0 x 10^{12} gc/ml. Dilutions reported are final. 100 nL of virus was injected into each of two to four locations positioned ~500 µm apart in primary visual cortex of TLX3-Cre mice. High magnification apical tuft imaging (Fig. 3) was performed on a commercial two-photon microscope (Neurolabware) using

a Coherent Chameleon Discovery laser and a Nikon 16x 0.8NA objective. In some experiments, an electrically tuneable lens (Optotune) was used to extend the length of dendritic branch simultaneously imaged. Imaging was always performed at 13.2 Hz final framerate using 920 nm excitation. The experimental flow is illustrated in Extended Data Fig. 4. Lower magnification volume imaging of apical and basal dendrites (Extended Data Fig. 8) was performed using a 10x / 0.5NA objective (Thorlabs) mounted on a resonant scanning microscope (Ultima 2P plus, Bruker). An electrically tuneable lens (Optotune) was used to image 4 planes at 24 Hz total frame rate using 920 nm excitation.

Two-photon optogenetic stimulation and dendritic imaging. We developed a new strategy for simultaneous ultra-sparse two-photon dendritic imaging in V1 and two-photon optogenetic stimulation in LM. Expression of calcium indicator and opsin were achieved by injecting the same virus mixtures and dilutions as above for two-photon optogenetic stimulation during population imaging, and dendritic imaging of apical tufts with ultra-sparse expression, with one difference. Expressing calcium indicator in LM neurons causes their axons to fluoresce in layer 1 of V1, interfering in sparse imaging of the apical dendrites of V1 neurons. To avoid this problem, the calcium indicator virus injections were targeted to V1 only, using blood vessel patterns as a guide. The opsin virus injections were targeted to LM only to avoid unintended activation of V1 neurons. The expression locations were later confirmed using retinotopic mapping. Experiments were performed using the same equipment as the two-photon optogenetic stimulation and population imaging experiments above, with a 10X 0.5 NA objective. An image of the brain surface over the two-photon FOV was affine transformed onto the brain surface image obtained previously in widefield intrinsic imaging. The widefield retinotopic map was then used to assign a retinotopic location for each position in the two-photon field of view. For the experiments that produced the non-specific suppression results shown in Figure 4a-d, for every dendrite recorded, 9 groups consisting of 25 targets each were stimulated for 15 to 25 trials (mean 23) with a photostimulation duration of 250 ms. In feedback-recipient spine detection experiments that produced at least one spine, between 308 and 2994 targets (mean 2146) were assigned as a grid in LM, overlapping the retinotopic location of the imaged neuron in V1, also determined from the widefield map. Targets spanned 2 z-depths, when C1V1 expression was restricted to layer 5 using TLX-cre (6 spines, 5 recordings,

2 animals), or 4-6 z-depths, when C1V1 expression was cre-independent and spanned the depth of LM (30 spines (28 spines, 21 recordings, 9 animals). Targets were stimulated in random groups of 8 to 25 targets (mean 22), with each group stimulated only once. 420 to 1260 unique groups (mean 1066) were used per experiment, where every target participated in 8 to 16 groups (mean 12). Stimulation was performed with 12-16 mW per target every 1.25 (21 recordings) or 2 (5 recordings) seconds and lasted 500 ms. The imaging and stimulation scan paths were configured to be parfocal, with the SLM addressing light to stimulate spots both above and below its focal plane. The imaging plane was moved along the z-axis to image either somatic or dendritic signals using an electrically tuneable lens. Dendritic imaging fields-of-view spanned 80 to 150 µm to a side. Responses were recorded for 15 to 25 minutes using 30 to 50 mW average power, and imaging data was rigidly registered as it was acquired to correct for motion artifacts online.

Procedures for online detection of feedback responsive spines. Feedback inputs in visual cortex are known to make contacts with both apical and basal dendrites of L5 pyramidal neurons[4,65,66]. We therefore searched for feedback-responsive spines in apical dendrites using the following strategy. The registered recordings and their average images were used to place small elliptical ROIs over all protrusions from the dendrite that could represent a spine. ROIs were assigned and fluorescence extracted using ImageJ. These traces were transformed to $(F- F_0)/ F_0$ where F_0 was defined as the 10th percentile of a 90 second moving window. A stimulus response for each ROI on each trial (ΔR) was calculated by averaging fluorescence in the 9 frames prior to each stimulation and subtracting it from the average fluorescence in the 7 frames after the offset of each stimulation, avoiding any stimulation artifact. Independent spine activity was used to identify spines that were potentially driven by stimulation. ΔR for each spine across trials was compared to the average ΔR across all spines (ΔR_{mean}). As most activity was correlated across spines, these plots often contained diagonally extended distributions of data (Extended Data Fig. 9d). Independent spine activity was visible as a cloud of points with high ΔR, and ΔR_{mean} around zero. For each spine, the group of targets stimulated on trials that passed a threshold set on ΔR but stayed below a threshold on ΔR_{mean} were identified. If any targets were stimulated on more than 20% (reliability threshold) of these trials, it was further collected for inspection of all the trials on which that target was stimulated, regardless of whether it generated

independent activity. This analysis was then repeated iteratively, while varying thresholds set on ΔR (mean+0.5*SD to 3*SD), ΔR_{mean} (mean+0.5*SD to 1.5*SD), and the % reliability (10 to 20%). This process reduced the number of possibly effective target-spine combinations to a number that could be visually inspected online. Among these possible connections the 1 to 15 (mean 8.3) most promising candidates were selected based on the overall reliability and temporal profiles of the responses. New stimulation groups composed of these targets were designed to confirm if any are indeed connected. In early experiments (n = 2) these confirmation blocks were composed of 20 minutes of recording where 22 random combinations of the selected targets were stimulated, and the experiment ended there. Data from these confirmation blocks were used for the boosting analysis in Fig. 4 in these cases. It was found that most selected targets were not effective in driving spine activity but a small number were. Therefore in later experiments spine signals from shorter, five to ten minute confirmation blocks were analyzed online, and spines that were reliably responsive to stimulation identified. New target groups were then designed to stimulate only those confirmed target-spine combinations, either with or without additional visual stimulation. These data were then used for the boosting analysis. In a subset of experiments (n = 16) the experiment was started by mapping receptive fields using sparse noise stimulation and somatic imaging. When both a confirmed target-spine combination as well as a receptive field were obtained in the same neuron, feedback stimulation was combined with presentation of an inverse visual stimulus (as in Fig. 3) centered on that neuron's RF. In another subset of experiments (n = 4) we also delivered sparse noise stimuli during feedback stimulation. These data are not shown separately.

Semi-sparse dendritic imaging. Semi-sparse expression of calcium indicator was achieved (Extended Data Fig. 6, 7, 11) using the virus mixture: AAV2/1-*Synapsin1*-FLEX-GCaMP7s (gift of Douglas Kim & GENIE Project, Addgene viral prep #104491-AAV1) diluted 1:7 from stock concentration of 1.5 x 10^{13} gc/ml and AAV2/1- or AAV2/9-*CAG*-FLEX-tdTomato (gift of Edward Boyden, Addgene viral prep # 28306-AAV9) diluted 1:150 from stock concentration of 2.1 x 10^{13} gc/ml. 20-50 nL of virus was injected into each of four locations ~500 µm apart in primary visual cortex of TLX3-Cre mice. Imaging was performed using the same setup as for apical tuft imaging (above). An electrically tuneable lens was used for volume imaging, with two planes positioned

in layer 5 to capture somata, and two imaging planes around the bifurcation of apical dendrites at the layer 1 to layer 2/3 transition[67]. Imaging was performed at 6.6 Hz final framerate per plane using 920 nm excitation.

Dual-color two-photon imaging. Simultaneous expression of red calcium indicator[68] and green GABA indicator[69] was achieved using the virus mixture: AAV2/1-*Synapsin1*-FLEX-NES-jRGECO1a (Addgene 100853) diluted 1:2 from stock concentration of 2.7 x 10^{13} gc/ml, and AAV2/1-*CAG*-FLEX-iGABASnFR.F102G (gift of Loren Looger, Addgene 112167, viral prep by Charité - Universitätsmedizin Berlin Viral Core Facility VCA-148b) diluted 1:2 from stock concentration of 5.1 x 10^{12} gc/ml. 500 nL of virus was injected into 2 locations in V1 positioned 1 mm apart. Simultaneous expression of red calcium indicator and green glutamate indicator[70] was achieved using the virus mixture: AAV2/1-*Synapsin1*-FLEX-NES-jRGECO1a (gift of Douglas Kim & GENIE Project, Addgene viral prep 100853-AAV1) diluted 3:4 from stock concentration of 2.7 x 10^{13} gc/ml mixed with AAV2/1-*CAG*-FLEX-SF-iGluSnFR-A184S diluted 1:4 from stock concentration of 1-5 x 10^{12} gc/ml (gift of Jonathan Marvin and Loren Looger). 200 nL of virus was injected into each of four locations positioned ~300 µm apart in primary visual cortex of TLX3-Cre mice. Imaging was performed using the same equipment as for dendritic imaging, with the addition of a Coherent Fidelity-2 fiber laser for excitation of jRGECO1a at 1070 nm. Lasers were co-aligned through one scan path and total power was kept below 100 mW. Fields of view were 250 µm to 400 µm wide. Volume imaging was performed using either a piezoelectric objective positioner (Physik Instrumente) or an electrically tuneable lens (Optotune). When using a piezo one plane was acquired in layer 5 and one plane in layer 1. Layer 1 imaging planes were positioned 30 to 100 µm below the pia. When using an ETL two planes were acquired in each layer. Imaging was performed at 6.6 Hz final framerate per plane.

Visual stimuli: receptive field mapping. Visual stimuli were generated using Psychophysics toolbox and synchronized to imaging data post-hoc using MATLAB or LabVIEW. After recovery, every animal underwent one preparatory wide-field imaging session where retinotopic mapping was performed with drifting or flashing bars[71]. Widefield imaging was performed using calcium fluorescence for all animals except for those used in the two-photon optogenetic stimulation during dendritic imaging experiments. These animals had calcium indicator expression restricted to LM only.

Therefore we used intrinsic signals obtained under anesthesia to produce retinotopic maps. This allowed localization of LM and V1 to guide the appropriate placement of two-photon imaging fields-of-view. Ultra-sparse apical tuft imaging experiments were started with widefield-map guided FOV placement and proceeded with receptive field mapping using forward correlation. The stimulus used here was an 8 by 8 grid of 8 degree squares which transitioned from gray to black to white and back at 2 Hz for 2 seconds, one at a time on a gray background. Squares were visited in pseudorandom order, with a 1 second inter trial interval for a total of 8 times per square in one ten minute run. Receptive fields were calculated online by averaging deconvolved responses to each grid position, using data from one to three runs. Ultra-sparse volume imaging experiments (Extended Data Fig. 8) were started with receptive field mapping using reverse correlation of responses to 40 minutes of 5% sparse noise stimuli composed of 6-7 degree squares in a 6 by 6 grid updated at 4 Hz. In optogenetic stimulation during population imaging, semi-sparse dendritic imaging and dual color imaging experiments, two preparatory imaging sessions were performed: one widefield imaging session and one two-photon imaging session to produce retinotopic maps at cellular resolution. In these cases retinotopic mapping was performed with a 5 % sparse noise stimulus composed of 6-7 degree squares in a 10 by 10 grid, where randomly chosen squares transitioned at 4 Hz from gray to white or gray to black. Between 30 and 60 minutes of data were obtained. For optogenetic stimulation during population imaging, these data were used to build cellular resolution maps to guide stimulation group positioning and analysis. For the remaining experiments this preparatory session allowed approximate positioning of visual stimuli for each field-of-view. Each experimental session of semi-sparse dendritic imaging and dual-color imaging experiments was ended with 30 minutes of sparse noise stimulation to map receptive fields precisely. Receptive fields were calculated offline and neurons included or excluded from consideration based on how well the stimuli aligned with their receptive fields. For two-photon optogenetic stimulation during dendritic imaging, widefield retinotopic maps were used to position stimulation targets and the recorded neurons in the visual field as LM neurons did not express indicator.

Visual stimuli: drifting gratings. Visual stimuli were delivered with spherical correction applied[71]. In optogenetic stimulation experiments, visual responsivity was determined prior to stimulation group assignment using full field sinusoidal gratings of

0.02 or 0.08 cycles per degree (cpd) spatial frequency drifting in one of 8 directions (0º, 45º, 90º, 135º, 180º, 225º, 270º, 315º) at 2 Hz temporal frequency. During stimulation, a full field grating was displayed (0.05 cpd, 2 Hz) drifting in one of four directions: 0º, 90º, 180 º, 270 º for two seconds, followed by a four second baseline period. In ultra-sparse imaging experiments (Fig.3 and Extended Data Fig. 8), five different shapes of sinusoidal grating (0.02 - 0.08 cpd, 2 Hz, 8 directions) were used as stimuli: an 8º Gabor patch, a 16º Gabor patch, an "inverse" stimulus consisting of a 16º inverse Gaussian transparency mask on a full field sinusoidal grating background, an "annulus" consisting of an 16º degree inner inverse Gaussian mask and a 28º degree outer Gaussian mask, and finally a full field stimulus. Stimuli were on for one second, followed by a 2.5 second baseline period. In semi-sparse dendritic imaging experiments (Extended Data Figs. 6, 7, 11), Gabor patches (2 Hz, 0.05 cpd, 4 directions) of six sizes (5º, 10º, 20º, 40º, 60º and full field) were used. For dual color GABA-SnFR experiments either a 20º Gabor or full field gratings (2 Hz and 0.05 cpd, 8 directions) were used. For dual color Glu-SnFR experiments only full field gratings (2 Hz, 0.08 cpd, 8 directions) were used. In semi-sparse dendritic imaging and dual-color imaging experiments stimuli were displayed for one second and followed by a 1.5 second baseline period. In dual color imaging experiments, the red channel of the monitor used for stimulation was turned off to avoid imaging artifacts. Stimuli were delivered using two separate monitors: ACER B276HL, 1920 x 1080 px, 60 Hz, for two photon stimulation and ultra-sparse volume imaging and ASUS VG278HV, 1920 x 1080 px, 144 Hz, for all other experiments. Monitors were positioned 20 cm away from the mouse, at approximately 30º to the mouse's midline in the right hemifield. All sinusoidal gratings were 62% contrast.

Calcium imaging data pre-processing. Two-photon calcium imaging data were motion corrected, segmented and fluorescence deconvolved where indicated using Suite2p[72] in all experiments except all-optical spine mapping, where ImageJ was used for online ROI selection Deconvolution time constants were measured from the data. Data are presented as mean ± s.e.m. unless otherwise indicated.

Receptive field calculation. For offline (post-experiment) sparse noise receptive field mapping, neuropil-subtracted and deconvolved event traces were used. Event traces were denoised by thresholding at twice their standard deviation over their mean. Event

triggered stimulus ensembles were generated for every neuron by collecting the stimuli that preceded each event in a two second period and weighting those stimuli by the size of each event they preceded. The mean over event triggered stimulus ensembles were calculated for that two second window and the value in each stimulus frame and sparse noise grid position (10*10) was expressed as a Z-score over all stimulus frame and grid position combinations and median filtered within frame. A neuron's retinotopic preference was determined by the location of the maximum Z-score in a 600 ms window positioned over the peak of the event triggered average over time. This analysis was performed separately for light increments and decrements to get ON and OFF receptive fields. ROIs that failed to produce a maximum Z-score of five in either ON or OFF maps were excluded when making maps for two-photon stimulation experiments, and a maximum Z-score of two when including neurons for analysis in semi-sparse dendritic imaging. These thresholds were chosen by inspection and varied because variability in the data differed based on magnification of imaging. If both stimulus types were above threshold, retinotopic preference was computed as a weighted average of the two. For semi-sparse dendritic imaging experiments, neurons were further included for analysis based on the proximity of their receptive fields to the center of sinusoidal gratings displayed. The results were robust to changing this distance criterion, which is noted in the figure legends. For dual color imaging experiments, receptive fields were calculated for the population to confirm stimulation covered receptive fields but no exclusion criteria were applied. When map-making for two-photon photostimulation experiments, all neurons passing inclusion criteria were plotted in 3D such that their azimuth or elevation positions were the third dimension and their position in the FOV the first two. This cellular resolution retinotopic preference map was used to fit a smooth surface model that was used as a template for receptive field approximation in subsequent photostimulation experiments. Fitting of elevation and azimuth maps was done semi-automatically using a LOWESS surface fit (polynomial: linear, span: ~20, robust: bisquare) with cftool in MATLAB. The surface fits were used to infer receptive field positions for optogenetic experiment targeting and analysis after ROI coordinates were corrected for two effects. First, they were transformed to compensate for magnification changes associated with ETL engagement. Second, ROI coordinates were transformed to compensate for FOV changes across imaging sessions using affine transformations fit to match surface blood vessel patterns recorded in receptive field mapping sessions and

photostimulation sessions. Finally, we used the centroid locations of responding neurons to infer their azimuth and elevation preferences from the fitted surface models. For online receptive field mapping (both forward and reverse: Fig. 3, Extended Data Fig. 8) fluorescence was extracted by hand-drawn ROIs and then deconvolved. Receptive field position was decided visually, either at the location of the grid position eliciting the strongest response, or at the midpoint between ON and OFF positions eliciting the strongest responses.

Detection and mapping of two-photon stimulation responsive neurons. Segmentation results were manually inspected. Fluorescence traces from segmented ROIs were converted into a $(F-F_0)/F_0$ representation where F_0 was assigned as the 10^{th} percentile of all samples in a 2000 frame rolling window. The response of every neuron on every trial was represented as a signal-to-background ratio. First, the mean $(F-F_0)/F_0$ value in a 500 ms window after the end of photostimulation, or for visual stimulus only trials, after the samples that would have contained photostimulation if there were any, was computed (S_i, for trial i). Next, the mean $(F-F_0)/F_0$ value in a 500 ms window preceding visual stimulus onset was computed (B_i). Finally, the difference S_i-B_i was divided by the standard deviation of the B_i values over trials i-2, i-1 and i. We call this value R_i^{V+P} if during that trial both a visual stimulus and a photostimulus were delivered, and R_i^{V} if only a visual stimulus was delivered. For every stimulated cluster separately, significantly responsive neurons ('responders') were detected in two steps: First, after randomly sampling R_i^{V} trials to match the proportions of visual stimulus orientations between R_i^{V+P} and R_i^{V} trials, a Wilcoxon rank sum test was performed between the two trial-types (R_i^{V+P} and R_i^{V}). Running different random samples did not change the ultimate result. Second, multiple comparisons were corrected for by controlling the False Discovery Rate (FDR) using "mafdr" in MATLAB[73,74]. Results reported in Figures 1 and 2 are for an FDR of 2.5%. Our results do not depend on this threshold qualitatively (Extended Data Fig. 2). Next, the retinotopic preference of each neuron was estimated by interpolation from a smoothed retinotopic map generated in a previous imaging session (Fig. 1c, Fig. 2a) and aligned to the current session by affine registration of the brain surface blood vessel pattern. Any ROIs within 75 μm to either side of the V1/LM border estimated from this map were excluded from consideration. Next, in order to reveal the retinotopic distribution of detected responders, their retinotopic distance from the photo-stimulated location was

calculated as every responder's pair-wise retinotopic distance to all facilitated responders in the photostimulation area ('source neurons': Extended Data Fig. 2). All locally facilitated responders were considered to represent the stimulated retinotopic location, since both photo-stimulus driven and synaptically driven neurons constitute potential input sources to the other area. The resulting retinotopic distances of local responders are highly correlated with the absolute physical distances due to the retinotopic organization of visual cortex, whereas across area responders, even if retinotopically aligned, are a minimum of 150 μm, and in most cases hundreds of μm, away from the nearest source neuron. The resulting pairwise retinotopic distance probability distribution was binned into ~1.2 degree bins in visual space and normalized by a "null" distribution of the same kind, calculated by sampling all segmented neurons in the appropriate area 20,000 times (Extended Data Fig. 2). This normalization step was necessary because the availability of neurons at any given retinotopic distance from the locally facilitated responder population varied widely depending on expression density, the target locations, FOV size and positioning relative to the retinotopic map, and blood vessel distribution. This process was repeated separately for each target cluster (distributions for one example stimulation group shown in Extended Data Fig. 2b). Finally, these weighted probabilities were smoothed with a moving average of 5 bins and averaged across all stimulation groups (Fig. 2b). Bias between the topographic distribution of facilitated and suppressed responders was assessed by first computing for each stimulation group and each sign of influence, the centroids of the responder distributions obtained. A Wilcoxon rank-sum test was then performed between the centroid distributions of facilitated and suppressed responders across stimulation groups (Fig. 2d and Extended Data Fig. 2e). The strength and retinotopic spread of locally facilitated responders overlapped but were not identical in V1 and LM. To exclude the possibility that this accounted for the finding of a retinotopic difference between facilitated and suppressed neurons in the feedback direction, a subsampling procedure was performed to equalize the stimulation strength of the two directions, and retinotopic differences were re-assessed (Extended Data Fig. 3). We characterized all photostimulation groups by the number of local responders they generated ('stimulation strength'), and binned them by this metric (as illustrated in Extended Data Fig. 3a, left). The distributions of responder numbers differed between the feedforward (stimulate in V1) and feedback (stimulate in LM) direction. We next sampled the overlapping part of the two distributions: for

each bin that contained both V1 and LM stimulation groups, we randomly selected half the number of stimulation groups produced by the direction with fewer groups contributing to this bin (e.g. for a bin that contained 10 LM stimulation groups and 6 V1 stimulation groups, we randomly chose 3 LM and 3 V1 groups). The resulting resampled dataset contained the same number of V1 and LM stimulation groups, which also have the same ('matched') distribution of stimulation strengths (Extended Data Fig. 3a, right). From this matched dataset, we then re-computed the spatial organization of inter-areal influence (Extended Data Fig. 3b) and measured the difference between the centroids of across-border facilitated and suppressed neurons, separately for V1 stimulation groups (feedforward) and LM stimulation groups (feedback). This procedure resulted in a single value per direction, describing the retinotopic displacement between facilitation and suppression in this subsample of stimulation groups. Finally, we repeated this matching procedure 5000 times, selecting different random subsets of stimulation groups in the overlap of stimulation strength distributions, resulting in 5000 measurements of retinotopic displacement per direction. Extended Data Figure 3c shows the proportion of resampled datasets (out of the 5000) which produced a negative retinotopic difference between facilitation and suppression (suppressed responders at higher distances than facilitated responders), separately for each direction. In the feedback direction, a negligible proportion of these resamples ($p < 0.025$) produced such a negative difference, while a substantial proportion did in the feedforward direction ($p >> 0.025$). This indicates that the suppressive-center facilitating-surround profile of feedback was maintained in stimulation-strength matched samples, and was therefore not caused by differences in local stimulation strength. We then repeated this analysis, equalizing retinotopic spread and physical distance to across-area responders, neither of which abolished the effect (Extended Data Fig. 3).

Spatial extent and magnitude of photoactivation response in targeted area. The spatial extent of the photostimulation was quantified using an approach similar to previously published methods[64]. Responses to photostimulation were represented as a probability of obtaining "a significant trial" on a per neuron-target group combination (Extended Data Fig. 1a top), each R_i^{V+P} was represented as a Z-score relative to all R^V on a neuron-by-neuron basis. The number of trials crossing $Z = 1.64$ (single tail $\alpha = 0.05$) divided by the total number of trials yielded a response probability ($P_{Response}$).

All distances were measured as Euclidean distance in 3D. For axial measurements, only ROIs that had a target within one lateral HWHM (20.7 μm) were taken into account and the axial distance measured as the Z-offset to this target.

Effect of locomotion on population activity in V1 and LM. Styrofoam wheel motion was recorded using quadrature encoders (Kubler). Wheel displacement traces were differentiated and filtered with a 2.5 second moving average. Any trial of stimulus presentation in any experiment was assigned as a locomotion trial if running speed during that trial exceeded a threshold of 3 cm/s. Two datasets were combined for this analysis: visual stimulus only (V-type) trials from the functional connectivity experiments (n = 42 sessions) described above and V-type trials from a separate set of optogenetic connectivity experiments (n = 32 sessions), same as the above in every respect other than that we presented 20^{o} gratings during photostimulation instead of full field gratings. For this analysis the visual response of every recorded neuron was represented as the difference S_i-B_i as described above. Neurons were included for comparison based on retinotopic representation, visual response magnitude and reliability. Neurons were required to have retinotopic locations within 30 degrees of the stimulus center. For full field stimuli, the “center” was defined as the center of a very large Gaussian mask that was present over the stimulus but had negligible effect on the visible contrast. Neurons were required to pass a Wilcoxon signed rank test for visual responsiveness (B_i vs S_i) at p = 0.01 after Bonferroni correction, for at least one of the two stimuli displayed. In addition, neurons were required to have responded significantly on 30% of trials, with significance assessed using the threshold Z = 1.64 computed as above, under resolution measurement. To quantify the modulation of visually evoked responses with locomotion, a modulation index was computed per neuron as the difference between the mean response R = (S_i-B_i) on locomotion trials and the mean response on stationary trials, normalized by the mean response on stationary trials, (ΔResponse = (R_{run}-R_{sit})/R_{sit}) all for the preferred stimulus of that neuron. This value was averaged across all neurons in the same area within each session and a signed rank test performed between paired measurements of ΔResponse from LM and V1 across all sessions.

Ultra-sparse dendritic imaging: local events in apical tufts. To identify local events[26,75-78] in fine apical tuft dendrites of individual pyramidal cells expressing

GCaMP using our ultra-sparse expression strategy, imaging data was motion-corrected and downsampled four-fold in time to produce videos for inspection. Events were required to involve at least two spines active simultaneously, along with the dendritic branch between them, in the absence of simultaneous activity on the proximal end of the imaged dendrite. Based on these criteria two experimenters (MF and DH) blind to visual stimulus timing and type inspected all videos acquired independently, and then resolved discrepancies to arrive at consensus on the location and timing of dendritic events. ROIs were then hand drawn over the dendritic segments where events were identified, and over dendritic segments proximal to those, to compare integrated fluorescence and confirm the presence of an event in the distal ROI and absence of the event in the proximal ROI. Automated detection of these events proved challenging for several reasons. First, local events could occur anywhere along the dendrite and could have varying spatial extents. Second, local events had varying signal-to-noise and varying rise and decay times in comparison to global events recorded in the same branch. Third, many events were bright and clearly involved a single spine and its parent branch, but a second spine could not be unambiguously identified. Some of these events must also be true multi-spine events where the additional spines were not spatially resolved by our imaging, but we chose to be conservative and excluded any such events where a second spine was not identifiable. Together these features made the automated assignment of spatial ROIs, thresholds and other exclusion criteria a high dimensional task poorly constrained by the limited number of local events we found (Extended Data Fig. 4). To measure the spatial extent of local events, two separate ROIs were drawn over each local event location. One “mask” ROI encapsulated the entire branch with its spines, and the other “line” ROI traced a single pixel-wide line along the branch only. Fluorescence measured in each pixel in the mask ROI was averaged into the nearest pixel of the line ROI. The geodesic distance between each line ROI pixel and the most proximal line ROI pixel was measured. The mean fluorescence over time in each resulting 1-pixel wide geodesic distance bin was smoothed with a four second moving average and then converted to $(F- F_0)/ F_0$, where F_0 was assigned as the 10^{th} percentile of the fluorescence in a moving window 45 seconds wide. This trace was then normalized by the standard deviation of the whole trace over time. Fluorescence was also smoothed across space within individual time bins with a 2 μm moving average. Finally, the spatial profile of each event was calculated by averaging across identified

frames, and events aligned and normalized to their respective fluorescence peaks across space. An idealized local event was generated by averaging across events, which was then fit with the sum of three Gaussians.

Ultra-sparse dendritic imaging: volume imaging of apical and basal dendrites. Imaging data were motion-corrected offline using the two-step procedure of Suite2P version v0.9.2, and ROIs were hand-drawn to avoid cross-talk with nearby processes. For the 5 neurons that showed a significant positive effect, we confirmed that ROIs segmented and neuropil subtracted using Suite2P produced the same result. Visual responses were quantified as a peak difference in a seven frame (~1s) window starting three frames after visual stimulus onset in comparison to baseline measured in a four frame window ending one frame before visual stimulus onset. Responses were averaged across all apical dendritic ROIs (in the two superficial-most imaging planes) and all basal ROIs excluding the soma (in the deepest imaging plane). From this point on, only trials that produced a visual response in the average of basal ROI signals that was greater than 20% of peak response in the average of basal ROIs were included in the analysis to focus on global events, similar to the analysis for semi-sparse dendritic imaging. The ratios between the apical and basal responses were quantified trial by trial. Responses to the two Gabor stimuli were pooled to construct a low-surround stimulus class and responses to the inverse and full field stimuli were pooled for a high-surround class. The difference between the average ratios for these two stimulus classes was computed. To assess the significance of the ratio difference, the procedure was repeated 3000 times, with trials shuffled between the stimulus classes, replicating the number of trials obtained for each class. Neurons that produced a difference larger than 95% of shuffles were regarded as significant. To measure correlations between ROIs, the apical to basal ratios were computed taking the response of each apical ROI and comparing it to the average of all basal ROIs. This resulted in a vector of ratios for each apical ROI. The correlation between these vectors was computed for the last panel of Extended Data Fig. 8.

Semi-sparse dendritic imaging: relative modulation of apical trunks. After motion correction and segmentation, ROIs identified in layer 5 were included for analysis as “soma ROIs” if they produced a significant receptive field (see above), and were clearly a section through a soma and not an apical dendrite of a deeper soma. All ROIs

segmented from our second most superficial imaging plane, which was placed just below layer 1, were included for analysis as “dendrite ROIs.” Our most superficial imaging plane often extended into layer 1 where apical dendrites had already ramified and the density of fluorescent processes was high. These data were excluded to analyze only sections through apical dendritic trunks of pyramidal neurons, with the goal of coming as close as possible to imaging the nexus across a population with variable nexus locations. Connected somata and dendrites were identified by examining correlations between fluorescence traces as well as the deconvolved event traces for every possible pairing of soma and dendrite ROIs (Extended Data Fig. 7). Any pair that exceeded a fluorescence trace correlation of 0.45 and an event trace correlation of 0.25 was assigned as “connected.” These thresholds were found to provide a conservative decision criterion, as illustrated by the example in Extended Data Fig. 7. Somata and dendrites identified in this way were traceable through structural z-stacks, but not always unambiguously so, as even a slight density of expression commonly leads to crossings of neuronal processes at distances smaller than the imaging resolution. Changing the correlation thresholds to 0.55 (F) and 0.35 (events) did not alter the results qualitatively. Fluorescence traces were converted to $(F- F_0)/F_0$ where F_0 was assigned as the mean fluorescence of that ROI across the entire recording duration. To measure effect of visual stimulus size on dendritic activity, responses to the more effective orientation (2 directions) were used. The response of every ROI on every trial was quantified as a modulation from baseline, where the baseline was defined as the mean fluorescence in the three frames preceding stimulus onset and the response was defined as the mean fluorescence in the ten frames after stimulus onset. Next, the value for every trial was normalized by the peak fluorescence recorded from that ROI in any trial. Trials were then sorted and binned by the somatic activity level separately for each stimulus size. Binning was performed with 5% bin width, going from -40% of peak to 100% of peak. All trials from all neurons in each bin were then averaged to obtain one population level value each for soma and dendrite for each stimulus size and bin. Next, a 2-way ANOVA was performed on population data to determine the effect of somatic activity, stimulus size and their interaction on dendritic activity (Extended Data Fig. 6c). To ask if individual neurons showed dendritic size tuning, somatic influence was removed on a cell by cell and trial by trial basis. For this analysis, only trials where the soma was active to 20% or more of peak were included as the effects were visible at higher activity levels where

dendrites were more strongly activated, and responses were quantified as the peak fluorescence on a given trial relative to baseline, with the same time windows used above. To summarize and remove the relationship between somatic and dendritic fluorescence a linear model was fit to data from a single neuron across all stimuli and the residuals obtained for each trial. A 1-way ANOVA was then performed to ask if stimulus size had a significant effect on the residuals. Preferred size of dendritic residuals was taken as the size that produced the largest residual fluorescence value. Working on deconvolved events with event-wise analyses instead of fluorescence with trial-wise analyses, and alternative procedures for matching somatic activity across stimulus sizes produced qualitatively similar results. To measure the effect of locomotion on apical dendritic activity, a similar approach was used. First, data was binned and normalized within neuron to produce a normalized population average. These data were subjected to a 2-way ANOVA to determine the effect of somatic activity, locomotion and their interaction on dendritic activity. Next, locomotion effects were measured on a cell-by-cell basis after removal of somatic influence. This was done by fitting a linear model to data from a single neuron across all stimuli and behavioral states, obtaining the residuals of this fit for each trial, and performing a 2-way ANOVA on these data to determine whether locomotion, stimulus size or their interaction had a significant effect. Again, only trials where the soma was active to 20% or more of peak were included. Next, the average residual within stimulus and behavioral state category was computed for each neuron, and post-hoc tests were performed to ask if locomotion had a significant effect for each stimulus category separately. Stimuli were pooled as smaller than preferred, preferred, or larger than preferred. Preferred size was computed on data obtained during stationary states. Here also, using deconvolved events instead of fluorescence, and alternative methods to remove somatic influence produced the same qualitative results.

Dendritic imaging during two-photon stimulation: boosting analysis. A “boosting index” was calculated to ask if feedback stimulation caused calcium signals in a dendritic branch segment that extends beyond the feedback recipient spine itself. Two sets of two ROIs were drawn. One ROI of each set was placed on a reference branch of the same neuron, not carrying a stimulated spine. The other ROI of each set was placed distally on the stimulated branch, but excluded the identified feedback recipient spine itself. In cases where only one extended stretch of dendrite was imaged, the

reference ROI was placed proximally on the stimulated branch, as far as possible from the spine. The two sets differed in that the stimulated branch ROIs were drawn either relatively closer to or relatively farther from the stimulated spine. The distributions of shortest straight-line distance between the centroid of the stimulated spine and the nearest pixel of the stimulated branch ROI are shown in Extended Data Figure 10b. A boosting index was then calculated by taking the ratio of the post-stimulus fluorescence value in the stimulated branch ROI to that in the reference branch ROI. Boosting indices were calculated separately for trials where stimulation was performed and "blank" trials where no stimulation was performed and then compared across the trial types to ask if there was an effect of stimulation.

Dual-color two-photon imaging. Layer 5 segmentations were manually curated to remove poorly sectioned neurons. Data was acquired in 10 or 20 minute blocks of trials, and the first three trials excluded to remove a fast bleaching component. To represent population activity the deconvolved event traces were averaged across segmented ROIs. To represent apical and basal SnFR fluorescence, the fluorescence recorded across the entire FOV was averaged and converted to $(F- F_0)/ F_0$ where F_0 was calculated as the 10^{th} percentile of F across all time points separately for each acquisition block of 10 or 20 minutes. When two planes were acquired in each layer, the SnFR signals from the two planes within layer were averaged together. For the majority of iGluSnFR and all iGABASnFR sessions receptive fields were mapped with sparse noise stimuli to confirm the retinotopic representation was well stimulated by our monitor. For the remaining iGluSnFR sessions widefield retinotopic maps were used. The linear models presented in Fig. 6 were fit to unequal numbers of stationary and locomotion trials (stationary: 371 ± 143, locomotion: 364 ± 98 trials mean ± s.d.). Resampling to match trial numbers did not change the results qualitatively. We excluded sessions that contained less than 150 trials of locomotion. Models were highly significant, and accounted for a moderate amount of variance, with $R^2 = 0.292 \pm 0.17$ (mean ± s.d.) across 12 sessions. To assess the significance of interactions between locomotion and glutamate signals, we performed a Wald's model comparison test, where we compared the full model to a restricted model excluding both interaction terms. Four out of 12 sessions produced significance (solid points in Extended Data Fig. 11k) but most sessions had a trend.

References

51 Gerfen, C. R., Paletzki, R. & Heintz, N. GENSAT BAC cre-recombinase driver lines to study the functional organization of cerebral cortical and basal ganglia circuits. *Neuron* **80**, 1368-1383, doi:10.1016/j.neuron.2013.10.016 (2013).

52 Mayford, M. *et al.* Control of memory formation through regulated expression of a CaMKII transgene. *Science* **274**, 1678-1683, doi:10.1126/science.274.5293.1678 (1996).

53 Madisen, L. *et al.* Transgenic mice for intersectional targeting of neural sensors and effectors with high specificity and performance. *Neuron* **85**, 942-958, doi:10.1016/j.neuron.2015.02.022 (2015).

54 Goldey, G. J. *et al.* Removable cranial windows for long-term imaging in awake mice. *Nat Protoc* **9**, 2515-2538, doi:10.1038/nprot.2014.165 (2014).

55 Rickgauer, J. P., Deisseroth, K. & Tank, D. W. Simultaneous cellular-resolution optical perturbation and imaging of place cell firing fields. *Nat Neurosci* **17**, 1816-1824, doi:10.1038/nn.3866 (2014).

56 Packer, A. M., Russell, L. E., Dalgleish, H. W. & Hausser, M. Simultaneous all-optical manipulation and recording of neural circuit activity with cellular resolution in vivo. *Nat Methods* **12**, 140-146, doi:10.1038/nmeth.3217 (2015).

57 Carrillo-Reid, L., Yang, W., Bando, Y., Peterka, D. S. & Yuste, R. Imprinting and recalling cortical ensembles. *Science* **353**, 691-694, doi:10.1126/science.aaf7560 (2016).

58 Mardinly, A. R. *et al.* Precise multimodal optical control of neural ensemble activity. *Nat Neurosci* **21**, 881-893, doi:10.1038/s41593-018-0139-8 (2018).

59 Marshel, J. H. *et al.* Cortical layer-specific critical dynamics triggering perception. *Science* **365**, doi:10.1126/science.aaw5202 (2019).

60 Szabo, V., Ventalon, C., De Sars, V., Bradley, J. & Emiliani, V. Spatially selective holographic photoactivation and functional fluorescence imaging in freely behaving mice with a fiberscope. *Neuron* **84**, 1157-1169, doi:10.1016/j.neuron.2014.11.005 (2014).

61 Shemesh, O. A. *et al.* Temporally precise single-cell-resolution optogenetics. *Nat Neurosci* **20**, 1796-1806, doi:10.1038/s41593-017-0018-8 (2017).

62 Russell, L. E. *et al.* All-optical interrogation of neural circuits in behaving mice. *Nat Protoc*, doi:10.1038/s41596-022-00691-w (2022).

63 Robinson, N. T. M. *et al.* Targeted Activation of Hippocampal Place Cells Drives Memory-Guided Spatial Behavior. *Cell* **183**, 1586-1599 e1510, doi:10.1016/j.cell.2020.09.061 (2020).

64 Russell, L. E. *et al.* The influence of visual cortex on perception is modulated by behavioural state. 706010, doi:10.1101/706010 bioRxiv (2019).

65 Young, H., Belbut, B., Baeta, M. & Petreanu, L. Laminar-specific cortico-cortical loops in mouse visual cortex. *Elife* **10**, doi:10.7554/eLife.59551 (2021).

66 Coogan, T. A. & Burkhalter, A. Hierarchical organization of areas in rat visual cortex. *J Neurosci* **13**, 3749-3772, doi:10.1523/JNEUROSCI.13-09-03749.1993 (1993).

67 Beaulieu-Laroche, L., Toloza, E. H. S., Brown, N. J. & Harnett, M. T. Widespread and Highly Correlated Somato-dendritic Activity in Cortical Layer 5 Neurons. *Neuron* **103**, 235-241 e234, doi:10.1016/j.neuron.2019.05.014 (2019).

68 Dana, H. *et al.* Sensitive red protein calcium indicators for imaging neural activity. *Elife* **5**, doi:10.7554/eLife.12727 (2016).

69 Marvin, J. S. *et al.* A genetically encoded fluorescent sensor for in vivo imaging of GABA. *Nat Methods* **16**, 763-770, doi:10.1038/s41592-019-0471-2 (2019).

70 Marvin, J. S. *et al.* Stability, affinity, and chromatic variants of the glutamate sensor iGluSnFR. *Nat Methods* **15**, 936-939, doi:10.1038/s41592-018-0171-3 (2018).

71 Marshel, J. H., Garrett, M. E., Nauhaus, I. & Callaway, E. M. Functional specialization of seven mouse visual cortical areas. *Neuron* **72**, 1040-1054, doi:10.1016/j.neuron.2011.12.004 (2011).

72 Pachitariu, M. *et al.* Suite2p: beyond 10,000 neurons with standard two-photon microscopy. 061507, doi:10.1101/061507 %J bioRxiv (2017).

73 Benjamini, Y. & Hochberg, Y. Controlling the False Discovery Rate - a Practical and Powerful Approach to Multiple Testing. *J R Stat Soc B* **57**, 289-300, doi:DOI 10.1111/j.2517-6161.1995.tb02031.x (1995).

74 Storey, J. D. c. *J R Stat Soc B* **64**, 479-498, doi:10.1111/1467-9868.00346 (2002).

75 Kerlin, A. *et al.* Functional clustering of dendritic activity during decision-making. *Elife* **8**, doi:10.7554/eLife.46966 (2019).

76 Major, G., Polsky, A., Denk, W., Schiller, J. & Tank, D. W. Spatiotemporally graded NMDA spike/plateau potentials in basal dendrites of neocortical pyramidal neurons. *J Neurophysiol* **99**, 2584-2601, doi:10.1152/jn.00011.2008 (2008).

77 Polsky, A., Mel, B. W. & Schiller, J. Computational subunits in thin dendrites of pyramidal cells. *Nat Neurosci* **7**, 621-627, doi:10.1038/nn1253 (2004).

78 Losonczy, A., Makara, J. K. & Magee, J. C. Compartmentalized dendritic plasticity and input feature storage in neurons. *Nature* **452**, 436-441, doi:10.1038/nature06725 (2008).

Data Availability

Datasets supporting the findings are available from the corresponding authors upon reasonable request.

Code Availability

Custom code for SLM calibration and Near Automatic Photoactivation Response Mapping are available at https://github.com/llerussell/SLMTransformMaker3D and https://github.com/llerussell/Naparm.

Competing Interests

We declare no competing interests.

Extended Data Fig. 1 | Photoactivation parameters, response magnitude and reliability.

a, Spatial extent of two-photon optogenetic photoactivation. Top, response probability by distance from targeted locations. Curves obtained from the experiments that produced data in Figures 1 & 2. Bottom, pixelwise photostimulus-

triggered response averages of one example photostimulation group in three dimensions.

b, Response reliability of facilitated responders in the stimulated area (top, “local”) and in the other area (bottom, “across”) as a function of false discovery rate (n = 310 stimulation groups, two-sided Wilcoxon rank sum test). Boxes indicate median, 75th and 25th percentile, whiskers indicate upper and lower adjacent values.

c, Most locally facilitated responders are weakly activated, with a small number being strongly activated.

d, The number of facilitated and suppressed responders as a function of false discovery rate. Bar plots represent mean ± s.e.m, dots indicate individual stimulation groups (n = 130 in LM and 180 in V1). Statistical test used was a Wilcoxon signed rank test between facilitated and suppressed responder counts. Note that the y-axis was set to the 95th percentile of the data for FDR 0.1 to facilitate visualization.

Extended Data Fig. 2 | Topographic map weighting and dependence on FDR.

a, Un-weighted retinotopic distance distributions of responders. These distributions are averages across all experiments. Data shown in Figure 2c, d are weighted, where the responder retinotopic distribution obtained for each stimulation group is weighted by the corresponding “all neurons” distribution for that stimulation group.

b, Un-weighted distance distributions of responders (as in a) for one example stimulation group (across-area facilitated and suppressed followers after LM photostimulation).

c, Un-weighted distance distributions of locally facilitated responders and target locations. Dashed lines s.e.m. across stimulation groups.

d, Topographic biases do not depend on FDR. Top left, the difference between un-weighted retinotopic distance distributions for facilitated feedback responders and their corresponding “all neurons” distributions. Bias across distance changes gradually as a function of FDR. Right, the integral of the difference plotted on the left as a function of FDR (mean ± s.d., n = 129 stimulation groups).

e, Each dot is the centroid of the retinotopic locations of responders recruited by one stimulation group (only stimulation groups with ≥ 1 across border responder, Feedback: n = 51/74/103 groups (FDR 2.5%, 5%, 10%) facilitated, n = 64/90/106 suppressed; Feedforward: n = 42/63/112 facilitated, n = 61/83/116 suppressed). Responder distributions are displaced between facilitated and suppressed

responders in the feedback direction but not in the feedforward direction (see also Fig. 2; Wilcoxon rank sum test). This comparison remains significant across different FDR thresholds for feedback.

Extended Data Fig. 3 | Differences in stimulation do not account for across-border response topography.

a, Procedure for matching local facilitated responder numbers (top), retinotopic spread (middle) and across-area responder physical distances from target location (bottom). Left, distributions for all stimulation groups before matching, which was performed by randomly sampling the overlapping segment of the distributions. Right, distributions after matching (see Methods).

b, Across-border response topography in the feedback (left) and feedforward (right) direction computed from resamples (mean ± s.d. across samples). Relative patterns of facilitation and suppression are maintained (Fig. 2).

c, Proportion of resamples with a negative difference between centroids of weighted probability distributions for facilitated and suppressed neurons as a function of FDR. Negative difference indicates suppressed neurons displaced relative to facilitated.

d, Left, retinotopic distance of responder to target location as a function of physical distance of responder to target location. Right, density plot showing the availability of all neurons.

e, Retinotopic distance distributions of facilitated and suppressed responders more than 500 μm away from the target location.

f, Number of across-border facilitated (left) and suppressed (right) neurons as a function of the number of local responders.

g, Photostimulation response magnitude as a function of retinotopic distance for all responders at FDR = 2.5%. Response magnitude is the difference between mean responses to the V+P trials and V trials. There is no effect of distance on response magnitude (ANOVA, $p = 0.34$ facilitated, $p = 0.35$ suppressed). Solid lines indicate binned and averaged response magnitude.

h, Probability of a feedback stimulation group producing at least one suppressed, at least one facilitated and at least one of each type of responder. Probability of finding both is not significantly less than would be expected based on the individual rates (permutation test, $p = 0.22$).

Extended Data Fig. 4 | Apical tuft dendrite imaging experiments.

a, Example illustrating experimental workflow, which consisted of finding a sparsely labeled group of neurons, mapping visual receptive fields, tracing from the soma to apical tuft while imaging at 800 nm and finding a branch that was relatively uninterrupted by other processes before displaying visual stimuli relative to the known receptive field.

b, Visual stimuli used in this experiment.

c, Two additional examples of dendrites that produced independent events. Bottom example illustrates challenges to automated detection. Event #1 was included in our data as an independent event that clearly involved at least two distinct spines and the branch. Event #2 was similar to #1 but only one spine and the branch were visibly activated during this smaller magnitude event. Event #3 was a global event that happened to be larger magnitude in the distal ROI in comparison to the proximal ROI.

Extended Data Fig. 5 | Spatial scale of local events in apical tuft dendrites.

a, Two separate ROIs were drawn over each dendritic segment where events were identified. One “mask” ROI encapsulated the entire branch with its spines, and the other “line” ROI traced a single pixel wide line along the branch itself.

b, Fluorescence measured in each pixel in the mask ROI was averaged into the nearest pixel of the line ROI, along with all other mask ROI pixels for which that line ROI pixel was the nearest. The geodesic distance between each line ROI pixel and the most proximal line ROI pixel was measured.

c, Fluorescence over time and geodesic distance along an example dendrite. The mean fluorescence in each resulting geodesic distance pixel was smoothed with a 4 second moving average and then converted to $(F-F_0)/F_0$, where F_0 was assigned as the 10^{th} percentile of the fluorescence in a running window 45 sec wide. We then normalized this ΔF/F by the standard deviation of the whole trace to facilitate comparisons across experiments.

d, The spatial profile of fluorescence over geodesic distance averaged over the frames identified with red band in c.

e, As in c for another example neuron.

f, As in d for another example neuron.

g, The spatial profile of all identified events, aligned by their peak location and normalized to that value in gray, their average in blue.

h, Same data as in g, average ± s.d.

i, Average spatial profile is well fit by a 3-term Gaussian with full-width at half-maximum of 11.2 μm.

Extended Data Fig. 6 | Visual stimuli that recruit enhanced facilitating feedback preferentially drive dendritic activity.

a, Semi-sparse expression allows tracing of apical trunks to their parent somata.

b, Left, soma and dendrite regions-of-interest. Right, fluorescence from a connected soma and apical dendrite.

c, Population average dendritic fluorescence as a function of somatic fluorescence, for six stimulus sizes. Trials sorted by somatic activity level, binned in 5% increments, averaged across cells (n = 57 neurons with receptive fields <20^o from stimulus center, and size tuning ($p < 0.01$) with preference for 20^o gratings). Two-way ANOVA on population data to determine effect of somatic activity, stimulus size, and their interaction on dendritic fluorescence showed a significant effect of stimulus size, $F(5,131) = 5.96$, $p = 5x10^{-5}$, and a significant interaction, $F(5,131) = 4.74$, $p = 5x10^{-4}$.

d, Population average somatic and dendritic calcium fluorescence traces for different stimuli from one somatic activity bin, indicated in panel c.

e, Dendritic fluorescence as a function of stimulus size, averaged across neurons after effect of somatic fluorescence is removed on a cell-by-cell basis (residual after subtraction of fit to somatic fluorescence; Methods). One way repeated measures ANOVA on n = 57 neurons shows significant effect of size, $F(5,280) = 2.681$, $p = 0.02$. Post-hoc tests show residual at 5^o is significantly smaller than residuals at larger stimulus sizes (paired t-tests, $p<0.05$).

f Dendritic and somatic size preference. Dendrites prefer larger stimuli as a population (paired t: $p = 1x10^{-6}$). Data from n = 131 neurons with receptive fields <20^o from stimulus center, significant size tuning ($p<0.01$), and preferring 10^o ,20^o, 40^o or 60^o gratings. Data from 26 sessions in 9 mice. Dendritic preference computed from residuals as in e.

g, Schematic illustrating topographically offset feedback facilitating dendritic excitation during global events.

Extended Data Fig. 7 | Identifying connected soma-apical dendrite pairs with semi-sparse expression.

a, Correlation between the fluorescence traces (X) and between the deconvolved event traces (Y) for all possible pairs of somata and dendrites from one session. Dashed line: thresholds used to identify connected pairs.

b, Soma plane from this example session.

c, Two dendrite planes from same example session.

d, Fluorescence of the soma and dendrites highlighted by red circles. Both dendrites belong to circled soma, but only one pair makes it past the conservative thresholds.

e, Another example that illustrates variability in expression density. Denser end of the range we obtain still allows identification of apical trunk and nexus below layer 1.

f, Dendrite fluorescence as a function of soma fluorescence, n = 76 neurons (receptive field <10 degrees of stimulus center, preferring 10, 20, 40 or 60 degrees). Fluorescence was baseline-subtracted (F_0 = 10^{th} percentile in a 1 minute running window) normalized by its standard deviation over the whole recording duration and decimated to 1 Hz for this plot. Note that high fluorescence in the dendrite in the absence of high fluorescence in the soma is not a feature of the data.

Extended Data Fig. 8 | Modulation of global events in apical dendrites relative to basal dendrites by visual stimuli.

a, Receptive field mapping with sparse noise stimuli and example receptive field.

b, Left, schematic with volume imaging planes. Right, example neuron showing ultra-sparse expression. Isolated somata were identified, their receptive fields mapped, and apical dendrites traced. Visual stimuli (same as in Fig. 3) were then positioned relative to the receptive field.

c, Traces from different dendritic locations. Arrows highlight events with variable ratio of apical to basal fluorescence.

d, Top left, apical dendritic responses to inverse and full field stimuli. Bottom left, basal dendritic responses to same stimuli. Top right, apical dendritic responses to Gabor stimuli. Bottom right, basal dendritic responses to same stimuli. Each trace shows one trial, with fluorescence from all apical and all basal ROIs averaged to get one trace per compartment.

e, Same data as in d, averaged across trials (mean ± s.e.m.) with responses to Gabor stimuli in blue and responses to inverse and full field stimuli in red, separately for apical (top) and basal dendrites (bottom).
f, Top, distribution of apical-to-basal fluorescence ratios across trials for the two stimulus classes for one cell. Bottom, same data, comparing the real difference between the apical-to-basal fluorescence ratios (difference of means of histograms above) to the shuffling stimulus ID for the same trials.
g, Top, apical-to-basal ratio differences for 26 recordings. Significantly modulated neurons shown in dark gray. Dashed line shows mean of all cells. Bottom, for the five significantly positively modulated neurons recorded, the apical-to-basal ratio was computed individually for each apical ROI against the average of all basal ROIs. The correlation between the apical-to-basal ratios across apical ROIs, with correlation of trunk and tuft ROIs in red and the correlation of tuft ROIs in blue.

Extended Data Fig. 9 | Two-photon photostimulation-triggered spine mapping.
a, Example dendrite and ROIs used for spine fluorescence extraction. Same experiment as shown in Figure 4, where panel f shows a section of the FOV shown here at higher magnification.
b, Fluorescence from six example ROIs.
c, Photostimulation responses of example ROI #1 plotted against the mean photostimulation response across all spine ROIs. Trials that produced independent activity were identified as passing a threshold applied to signals from that spine and not passing a threshold applied to the average spine. Targets active on those trials, like the example target #1095 shown, were identified.
d, Four example spines from four recordings. Top, stimulation-triggered average image showing independently activated spines. Bottom, the stimulation triggered fluorescence traces from those example spines.
e, An example spine and stimulation target pair that were identified in two separate experimental sessions, 3 days apart.
f, Distribution of retinotopic and physical distances between effective target in LM and the parent soma of the responsive spine. Retinotopic distances were measured using widefield intrinsic imaging under anaesthesia and temporal retinotopic mapping (Kalatsky et al., 2003).

g, Retinotopic position of effective targets in LM plotted relative to the retinotopic position of the parent soma of the responsive spine, positioned at the origin.

Extended Data Fig. 10 | Branch-specific boosting analysis.

a, Two additional examples of branch-specific local events in response to photostimulation of identified presynaptic targets in LM. Left, average image of global events, showing stimulated (incl. spine) and reference branch ROIs. Middle, spines responsive to feedback. Right, average image of single trial showing branch-specific event.

b, Fluorescence extracted from those ROIs, showing the variability of stimulated vs reference branch signal strength and the branch-specific events driven by photostimulation, indicated by red bars.

c, Top, schematic illustrating ideal layout of ROIs used for boosting analysis. Bottom, distribution of minimum distances between stimulated branch ROIs and the identified feedback recipient spine.

d, Mean boosting indices for blank vs photostimulation trials. Each recording appears once for “near” ROIs and once for “far”. “Near” ROIs same as reported in figure 4. Filled circles are individually significant neurons (t-test, $p<0.05$). Right, same data plotted as a histogram of differences between boosting indices measured during stimulation and during blank trials.

e, Boosting index (difference between photostimulation and blank, same data as in Figure 4º) as a function of retinotopic distance between target location and parent soma location.

f, Schematic illustrating visual stimulation delivered simultaneously with feedback stimulation.

g, Boosting indices measured from Near ROIs while the visual stimulus was a gray screen. Left, scatter plot of indices measured on blank vs on stimulation trials. Right, same data shown as a histogram of differences between trial types.

h, Boosting indices measured from Near ROIs while the visual stimulus was an inverse grating positioned around the receptive field of the V1 neuron. Left, scatter plot of indices measured on blank vs on stimulation trials. Right, same data shown as a histogram of differences between trial types.

Extended Data Fig. 11 | Locomotion regulates feedback and dendritic excitability.

a, FOV for measuring modulation of visual responses in V1 and LM.

b, Locomotion facilitates visual responses more in LM than V1 (signed-rank test, 20^o: $p = 0.017$, full-field: $p = 0.042$).

c, Increased feedback predicts increased suppression for smaller stimuli, and increased suppression and facilitation for larger stimuli.

d, Dendritic fluorescence as a function of somatic fluorescence, during locomotion and stationarity (mean ± sem, n = 131 neurons). A 2-way ANOVA to determine effect of somatic fluorescence and locomotion on dendritic fluorescence shows significant interaction: $F(1,48) = 8.86$, $p = 0.0046$.

e, Change in dendritic response with locomotion (mean ± sem). For each neuron we removed the effect of somatic activity and categorized stimuli as smaller than preferred (paired t-test, $p = 0.003$,) preferred ($p = 0.112$), larger than preferred ($p = 0.067$).

f, Apical dendrites are suppressed by locomotion when small stimuli, but not larger stimuli, are presented.

g, Somatic size tuning during locomotion and stationarity (n = 131).

h, Somatic response modulation. (mean ± s.e.m., smaller than preferred: paired t-test, $p = 5.45 \times 10^{-7}$, preferred: $p = 0.32$, larger than preferred: $p = 0.002$).

i, Locomotion reduces somatic response to small stimuli but enhances response to large stimuli.

j, Top, strategy for dual-color input-output imaging. Bottom, stimulus-triggered average glutamate and calcium fluorescence during stationarity and locomotion (n = 12 sessions, 4 mice).

k, Interaction coefficients between locomotion and apical/basal glutamate from linear model (Methods). Basal coefficients are significantly above (t-test, $p = 0.01$), apical coefficients below zero ($p = 0.02$). Filled circles are sessions with individually significant effect of omitting interactions.

l, Locomotion-induced enhancement of feedback, suppression of apical dendrites and somata during presentation of smaller stimuli, and enhancement of basal inputs and somata for larger stimuli.

Extended Data Fig. 12 | Locomotion-induced changes in glutamate, calcium signals and their relationships.

a, Schematic illustrating dual-color expression strategy.

b, Basal glutamate fluorescence over entire FOV during stationary and locomotion periods, averaged over all trials in one session.

c, Apical glutamate fluorescence over entire FOV during stationary and locomotion periods, averaged over all trials in one session.

d, Population activity quantified as deconvolved events across all ROIs over entire FOV during stationary and locomotion periods, averaged over all trials in one session.

e, Raw traces of iGluSnFR fluorescence and deconvolved calcium signals summed across the population. Gray bars are visual stimulus.

f, iGlu-SnFR fluorescence in basal dendrites during the baseline period did not change with locomotion (n = 12 sessions in n = 4 mice, t-test, $p = 0.12$).

g, iGlu-SnFR fluorescence in apical dendrites during the baseline period did not change with locomotion (t-test, $p = 0.18$).

h, Deconvolved events during the baseline period did not change with locomotion (t-test, $p = 0.25$).

i, Stimulus evoked change in mean iGlu-SnFR fluorescence in the basal dendrite planes increased with locomotion (t-test, $p = 1.3 \times 10^{-6}$).

j, Stimulus evoked change in mean iGlu-SnFR fluorescence in the apical dendrite planes increased with locomotion (t-test, $p = 1.8 \times 10^{-5}$).

k, Stimulus evoked change in deconvolved events increased with locomotion (t-test, $p = 0.02$).

l, Three dimensional population level input-output function for one session.

m, Linear model fit to each session in order to measure the interaction between locomotion and basal and apical glutamate to population output gain.

n, Coefficients of the interaction show that locomotion and basal glutamate interact positively (t-test, $p = 0.01$), while locomotion and apical gain interact negatively (t-test, $p = 0.02$). Solid data points are sessions with individually significant interactions between running and glutamate (Wald test, $p < 0.05$, Methods).

Extended Data Fig. 13 | Locomotion suppresses spontaneous GABAergic signaling in layer 1 neurons but enhances sensory-evoked GABAergic signals.

a, Expression and excitation strategy for dual-color imaging.

b, Average iGABA-SnFR fluorescence (top) and jRGECO1a fluorescence (bottom) in a typical field-of-view (300 μm). Visual stimuli were 20^{o} or full field sinusoidal gratings and they produced qualitatively similar results.

c, Example raw trace of iGABA-SnFR fluorescence recorded over the entire field of view and averaged over two imaging planes in layer 1.

d, Mean GABA fluorescence over entire field-of-view during stationary and locomotion periods, averaged over trials in one session.

e, Mean GABA fluorescence over entire field-of-view during stationary and locomotion periods, averaged across n = 33 sessions.

f, Mean fluorescence during stationarity vs locomotion. Top, GABA fluorescence during baseline periods significantly decreased with locomotion (t-test, $p = 5.5 \times 10^{-5}$). Bottom, stimulus evoked (baseline-subtracted) GABA fluorescence significantly increased with locomotion (t-test, $p = 3 \times 10^{-7}$).

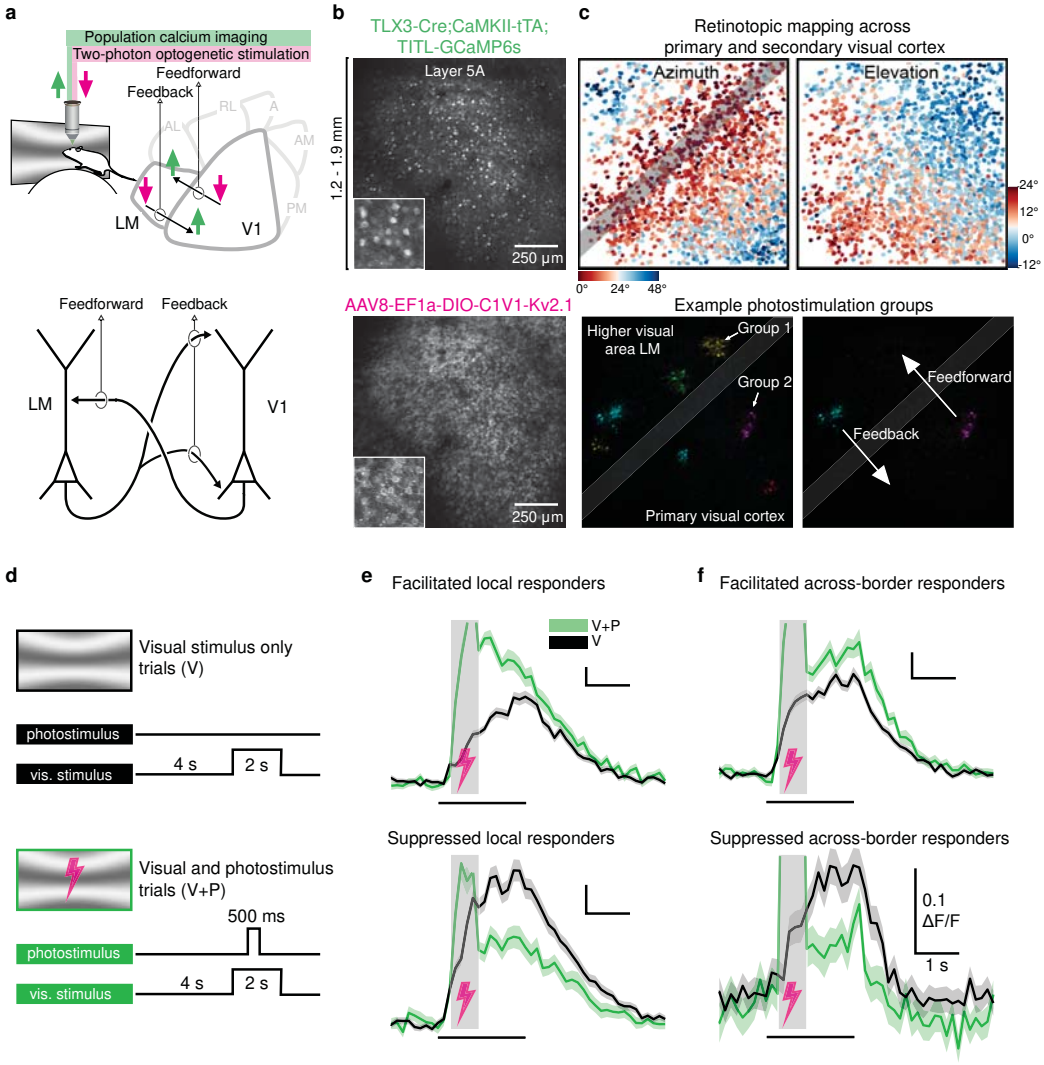
a
Population calcium imaging
Two-photon optogenetic stimulation
Feedforward
Feedback
RL
A
AL
AM
PM
LM
V1
Feedforward
Feedback
LM
V1
b
TLX3-Cre;CaMKII-tTA;
TITL-GCaMP6s
Layer 5A
1.2 - 1.9 mm
250 µm
AAV8-EF1a-DIO-C1V1-Kv2.1
250 µm
c
Retinotopic mapping across
primary and secondary visual cortex
Azimuth
Elevation
0°
24°
48°
24°
12°
0°
-12°
Example photostimulation groups
Higher visual
area LM
Group 1
Group 2
Primary visual cortex
Feedforward
Feedback
d
Visual stimulus only
trials (V)
photostimulus
vis. stimulus
4 s
2 s
Visual and photostimulus
trials (V+P)
500 ms
photostimulus
vis. stimulus
4 s
2 s
e
Facilitated local responders
V+P
V
Suppressed local responders
f
Facilitated across-border responders
Suppressed across-border responders
0.1
ΔF/F
1 s

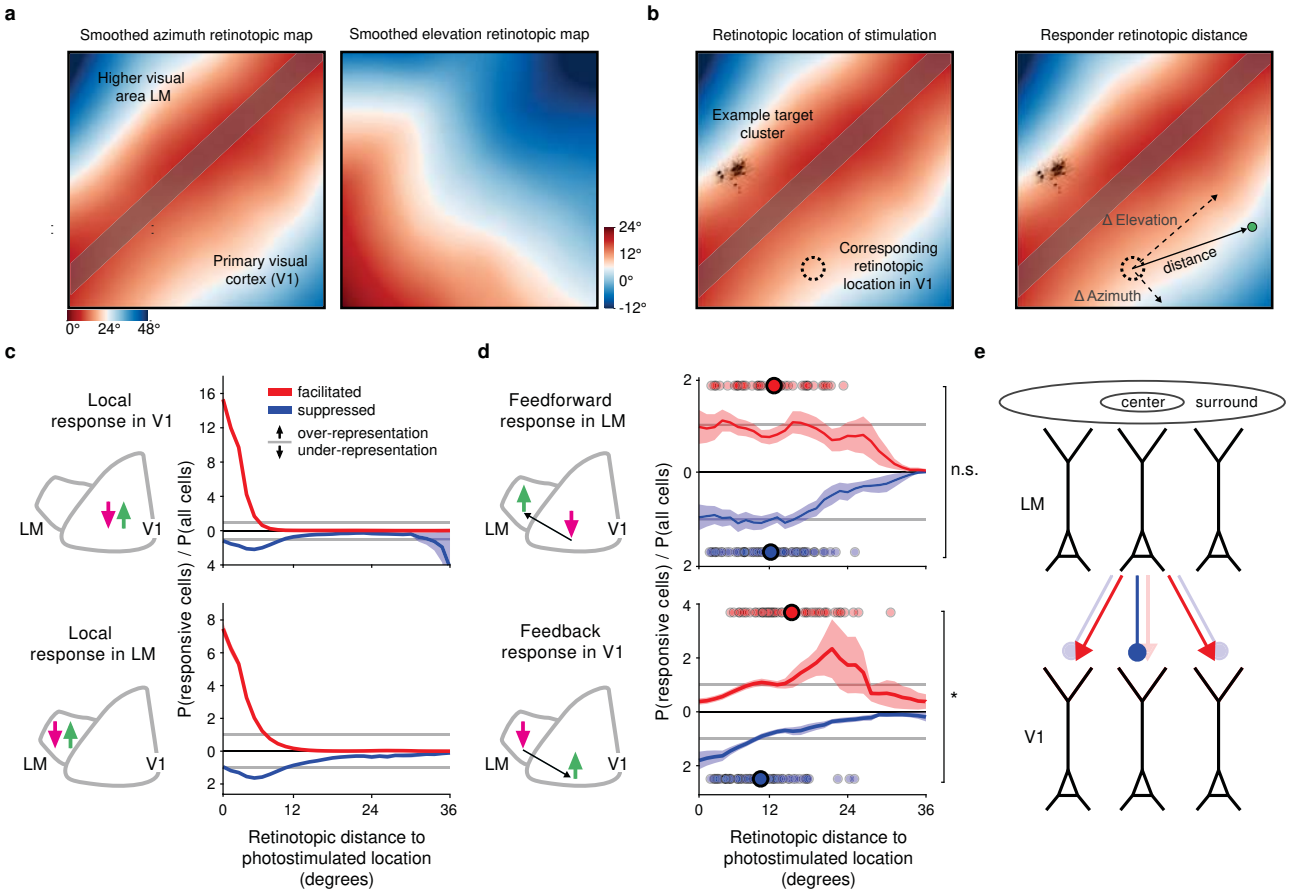
a
Smoothed azimuth retinotopic map
Smoothed elevation retinotopic map
Higher visual area LM
Primary visual cortex (V1)
0°
24°
48°
24°
12°
0°
-12°
b
Retinotopic location of stimulation
Responder retinotopic distance
Example target cluster
Corresponding retinotopic location in V1
Δ Elevation
distance
Δ Azimuth
c
Local response in V1
LM
V1
facilitated
suppressed
over-representation
under-representation
Local response in LM
P(responsive cells) / P(all cells)
Retinotopic distance to photostimulated location (degrees)
d
Feedforward response in LM
Feedback response in V1
n.s.
*
e
center
surround

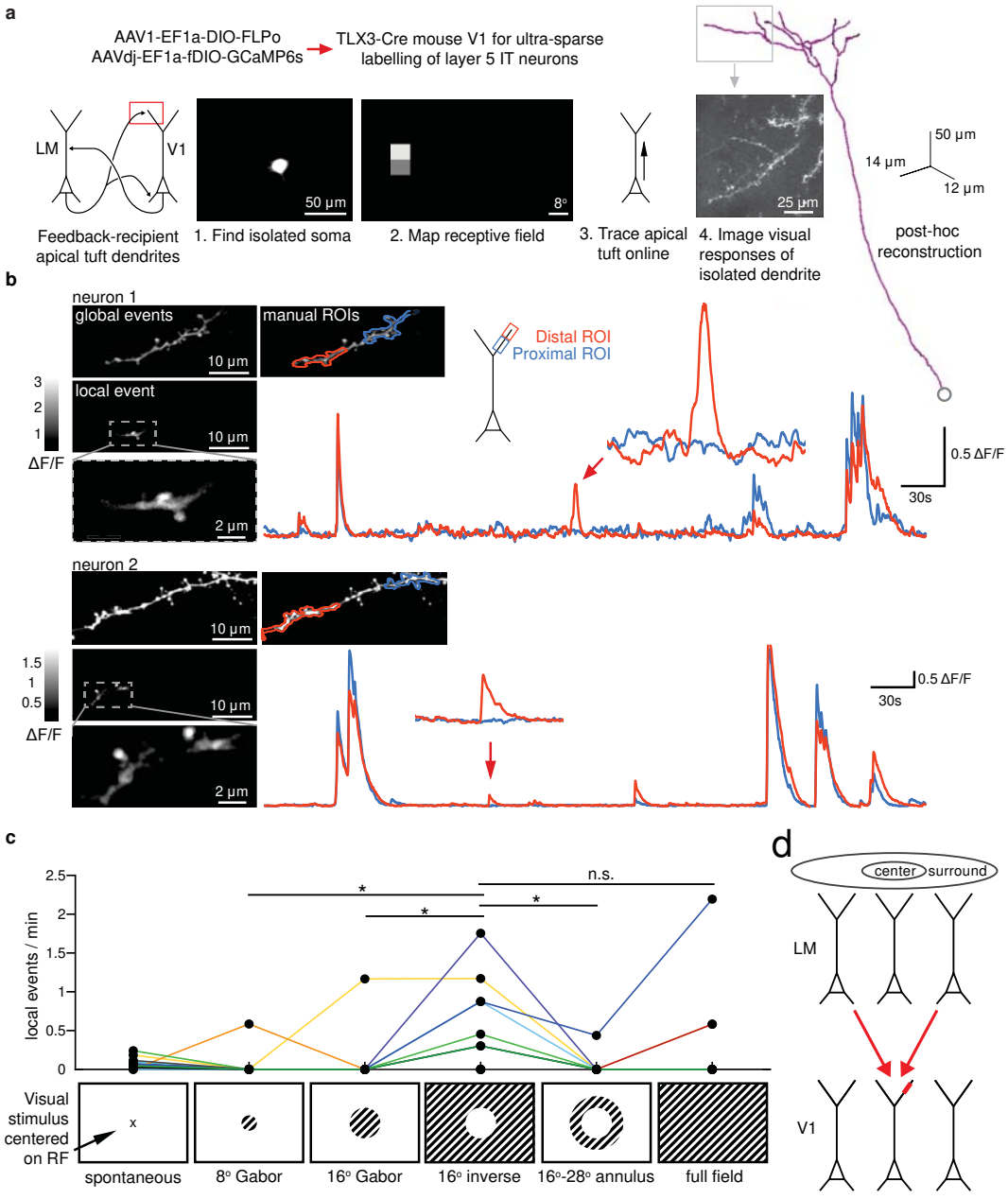
a
AAV1-EF1a-DIO-FLPo
AAVdj-EF1a-fDIO-GCaMP6s
TLX3-Cre mouse V1 for ultra-sparse labelling of layer 5 IT neurons
LM
V1
Feedback-recipient apical tuft dendrites
50 µm
1. Find isolated soma
8°
2. Map receptive field
3. Trace apical tuft online
25 µm
4. Image visual responses of isolated dendrite
50 µm
14 µm
12 µm
post-hoc reconstruction
b
neuron 1
global events
manual ROIs
10 µm
local event
2 µm
Distal ROI
Proximal ROI
3
2
1
ΔF/F
0.5 ΔF/F
30s
neuron 2
1.5
1
0.5
c
local events / min
2.5
2
1.5
1
0.5
0
n.s.
*
Visual stimulus centered on RF
x
spontaneous
8° Gabor
16° Gabor
16° inverse
16°-28° annulus
full field
d
center
surround
LM
V1

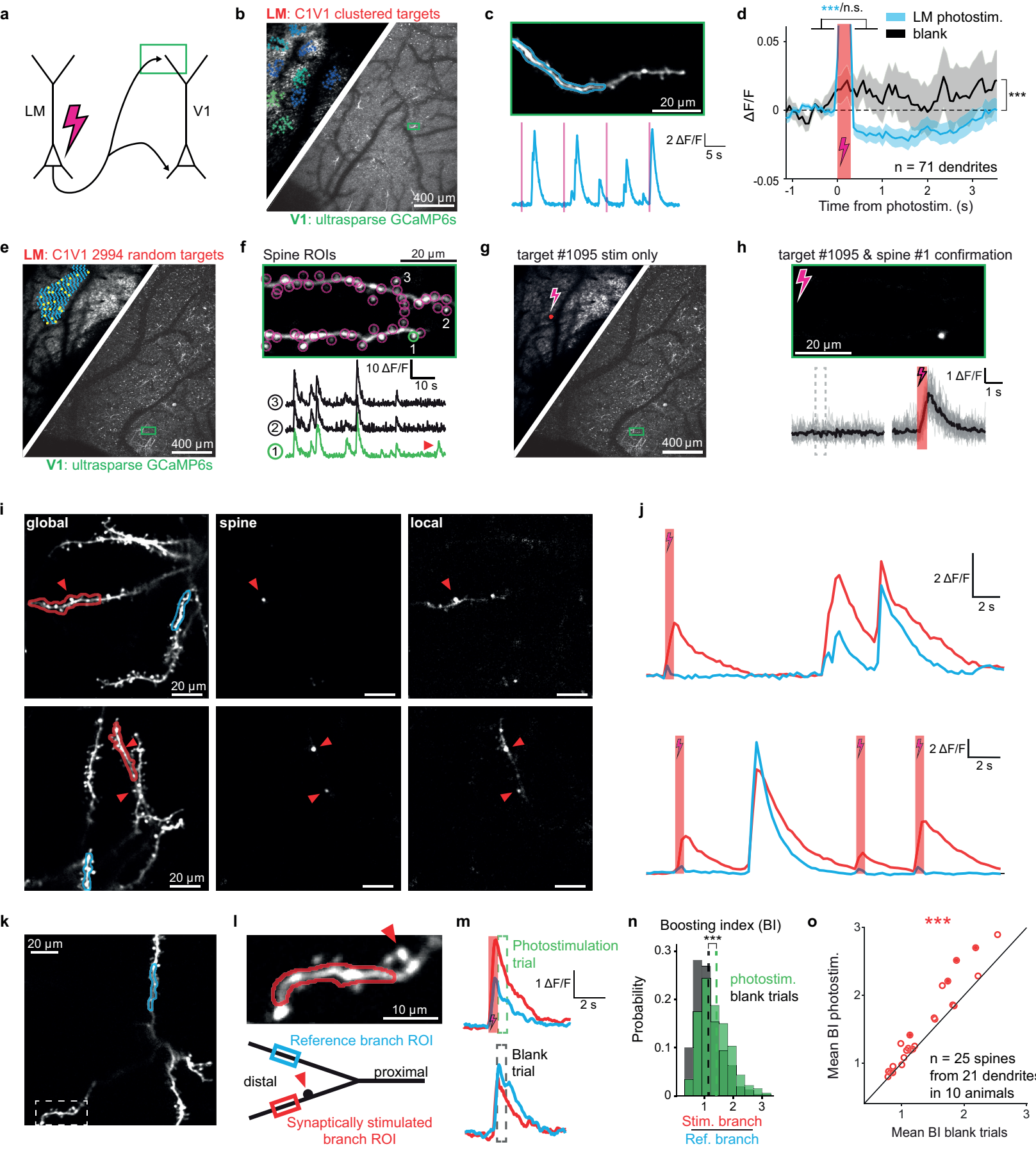
a
LM
V1
b
LM: C1V1 clustered targets
400 µm
V1: ultrasparse GCaMP6s
c
20 µm
2 ΔF/F
5 s
d
***/n.s.
LM photostim.
blank
0.05
0
-0.05
ΔF/F
***
n = 71 dendrites
-1
0
1
2
3
Time from photostim. (s)
e
LM: C1V1 2994 random targets
400 µm
V1: ultrasparse GCaMP6s
f
Spine ROIs
20 µm
3
2
1
10 ΔF/F
10 s
g
target #1095 stim only
400 µm
h
target #1095 & spine #1 confirmation
20 µm
1 ΔF/F
1 s
i
global
spine
local
20 µm
20 µm
j
2 ΔF/F
2 s
2 ΔF/F
2 s
k
20 µm
l
10 µm
Reference branch ROI
distal
proximal
Synaptically stimulated
branch ROI
m
Photostimulation
trial
1 ΔF/F
2 s
Blank
trial
n
Boosting index (BI)
***
0.3
0.2
0.1
0
Probability
photostim.
blank trials
1
2
3
Stim. branch
Ref. branch
o
***
3
2
1
Mean BI photostim.
n = 25 spines
from 21 dendrites
in 10 animals
1
2
3
Mean BI blank trials

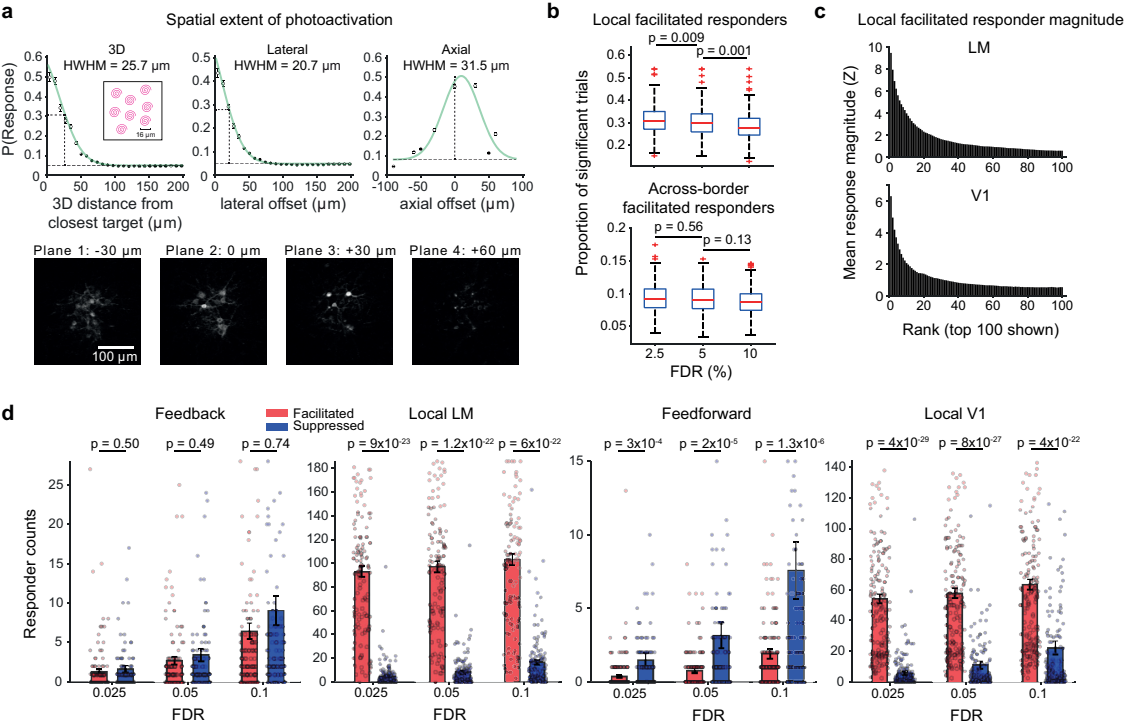
a
Spatial extent of photoactivation
3D
HWHM = 25.7 μm
Lateral
HWHM = 20.7 μm
Axial
HWHM = 31.5 μm
P(Response)
10 μm
3D distance from closest target (μm)
lateral offset (μm)
axial offset (μm)
Plane 1: -30 μm
Plane 2: 0 μm
Plane 3: +30 μm
Plane 4: +60 μm
100 μm
b
Local facilitated responders
p = 0.009
p = 0.001
Proportion of significant trials
Across-border facilitated responders
p = 0.56
p = 0.13
FDR (%)
c
Local facilitated responder magnitude
LM
V1
Mean response magnitude (Z)
Rank (top 100 shown)
d
Feedback
Facilitated
Suppressed
Local LM
Feedforward
Local V1
p = 0.50
p = 0.49
p = 0.74
p = 9x10-23
p = 1.2x10-22
p = 6x10-22
p = 3x10-4
p = 2x10-5
p = 1.3x10-6
p = 4x10-29
p = 8x10-27
p = 4x10-22
Responder counts
FDR

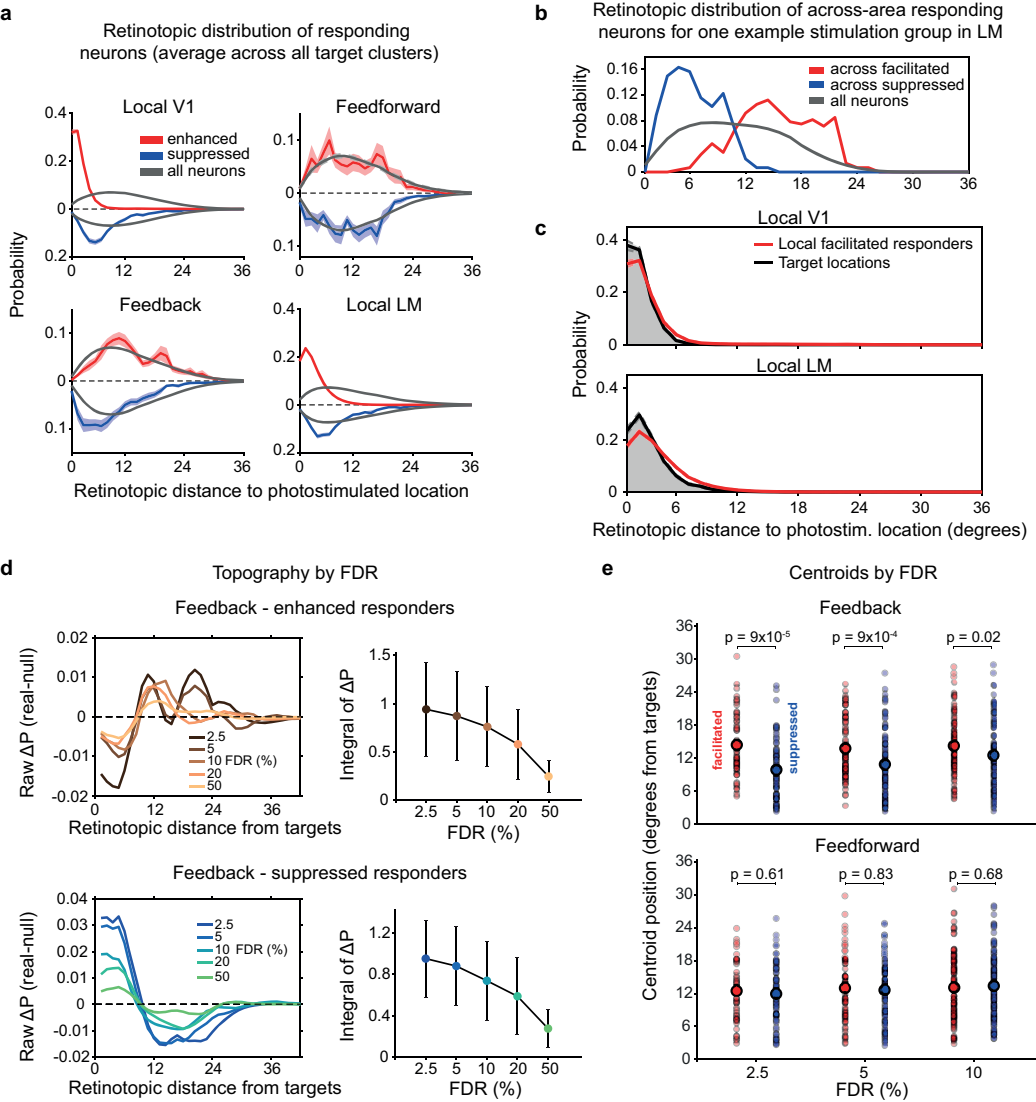
a
Retinotopic distribution of responding neurons (average across all target clusters)
Local V1
Feedforward
Feedback
Local LM
enhanced
suppressed
all neurons
Probability
Retinotopic distance to photostimulated location
b
Retinotopic distribution of across-area responding neurons for one example stimulation group in LM
across facilitated
across suppressed
all neurons
Probability
c
Local V1
Local facilitated responders
Target locations
Local LM
Probability
Retinotopic distance to photostim. location (degrees)
d
Topography by FDR
Feedback - enhanced responders
Raw ΔP (real-null)
2.5
5
10 FDR (%)
20
50
Retinotopic distance from targets
Integral of ΔP
FDR (%)
Feedback - suppressed responders
Raw ΔP (real-null)
2.5
5
10 FDR (%)
20
50
Retinotopic distance from targets
Integral of ΔP
FDR (%)
e
Centroids by FDR
Feedback
p = 9x10-5
p = 9x10-4
p = 0.02
facilitated
suppressed
Feedforward
p = 0.61
p = 0.83
p = 0.68
Centroid position (degrees from targets)
FDR (%)

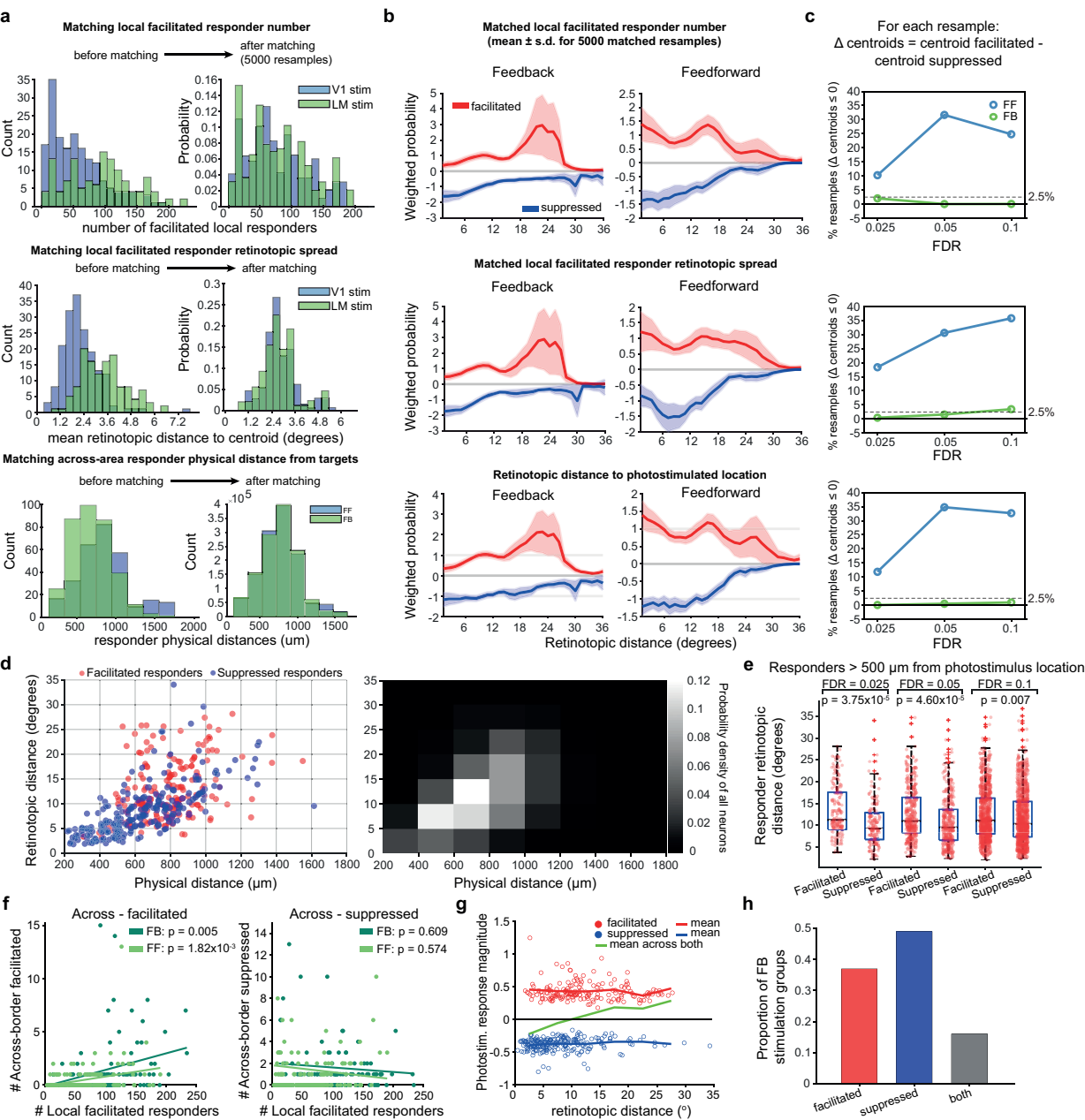
a
Matching local facilitated responder number
before matching
after matching
(5000 resamples)
Count
Probability
V1 stim
LM stim
number of facilitated local responders
Matching local facilitated responder retinotopic spread
mean retinotopic distance to centroid (degrees)
Matching across-area responder physical distance from targets
FF
FB
responder physical distances (um)
b
Matched local facilitated responder number
(mean ± s.d. for 5000 matched resamples)
Feedback
Feedforward
Weighted probability
facilitated
suppressed
Matched local facilitated responder retinotopic spread
Retinotopic distance to photostimulated location
Retinotopic distance (degrees)
c
For each resample:
Δ centroids = centroid facilitated -
centroid suppressed
% resamples (Δ centroids ≤ 0)
FF
FB
2.5%
FDR
d
Facilitated responders
Suppressed responders
Retinotopic distance (degrees)
Physical distance (μm)
Probability density of all neurons
e
Responders > 500 μm from photostimulus location
FDR = 0.025
FDR = 0.05
FDR = 0.1
p = 3.75x10-5
p = 4.60x10-5
p = 0.007
Responder retinotopic distance (degrees)
Facilitated
Suppressed
f
Across - facilitated
FB: p = 0.005
FF: p = 1.82x10-3
Across-border facilitated
Local facilitated responders
Across - suppressed
FB: p = 0.609
FF: p = 0.574
Across-border suppressed
g
facilitated
suppressed
mean
mean
mean across both
Photostim. response magnitude
retinotopic distance (°)
h
Proportion of FB stimulation groups
facilitated
suppressed
both

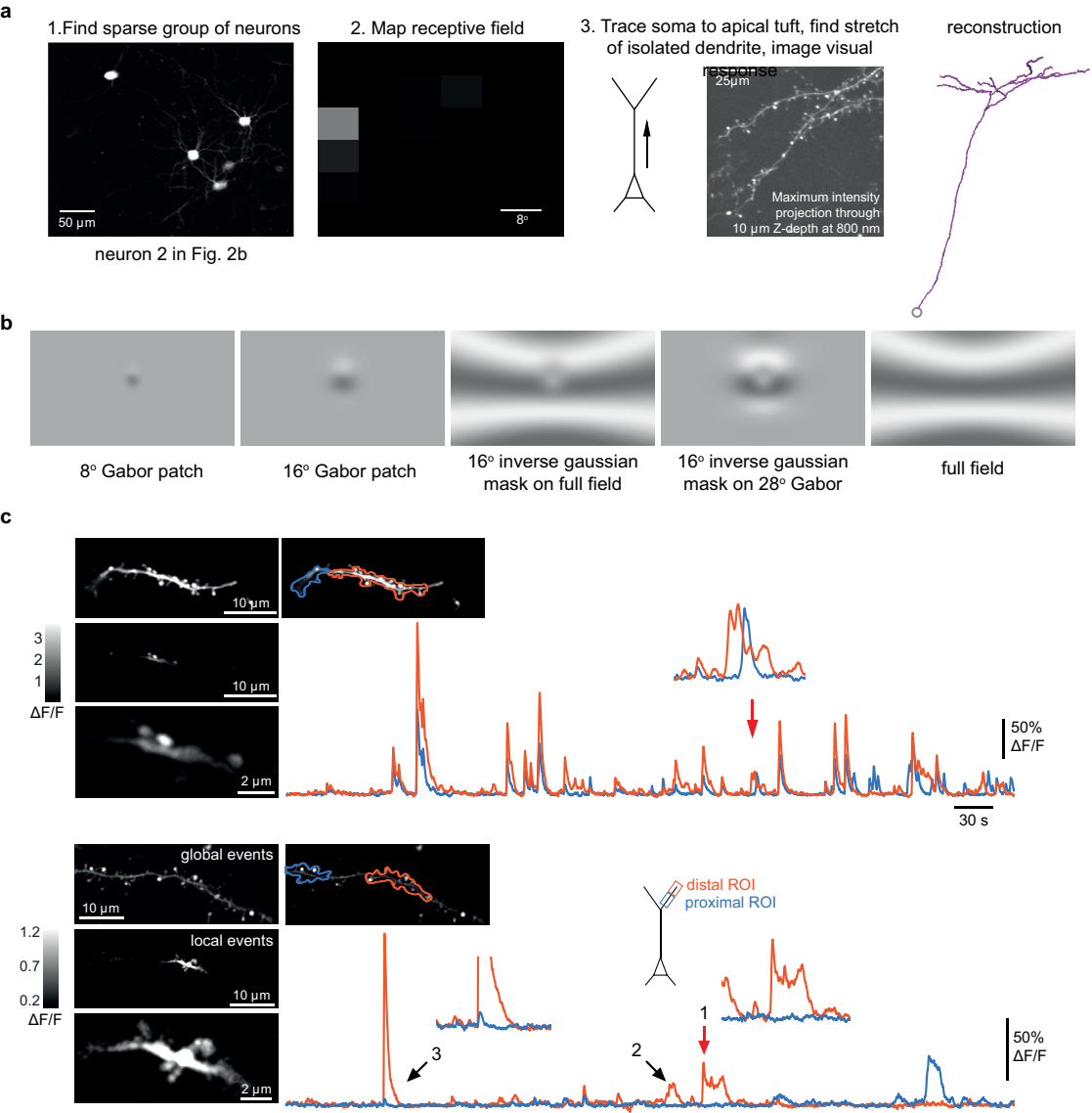
a
1.Find sparse group of neurons
50 µm
neuron 2 in Fig. 2b
2. Map receptive field
8°
3. Trace soma to apical tuft, find stretch of isolated dendrite, image visual response
25µm
Maximum intensity projection through 10 µm Z-depth at 800 nm
reconstruction
b
8° Gabor patch
16° Gabor patch
16° inverse gaussian mask on full field
16° inverse gaussian mask on 28° Gabor
full field
c
10 µm
3
2
1
ΔF/F
10 µm
2 µm
50%
ΔF/F
30 s
global events
10 µm
local events
10 µm
2 µm
1.2
0.7
0.2
ΔF/F
distal ROI
proximal ROI
1
2
3
50%
ΔF/F

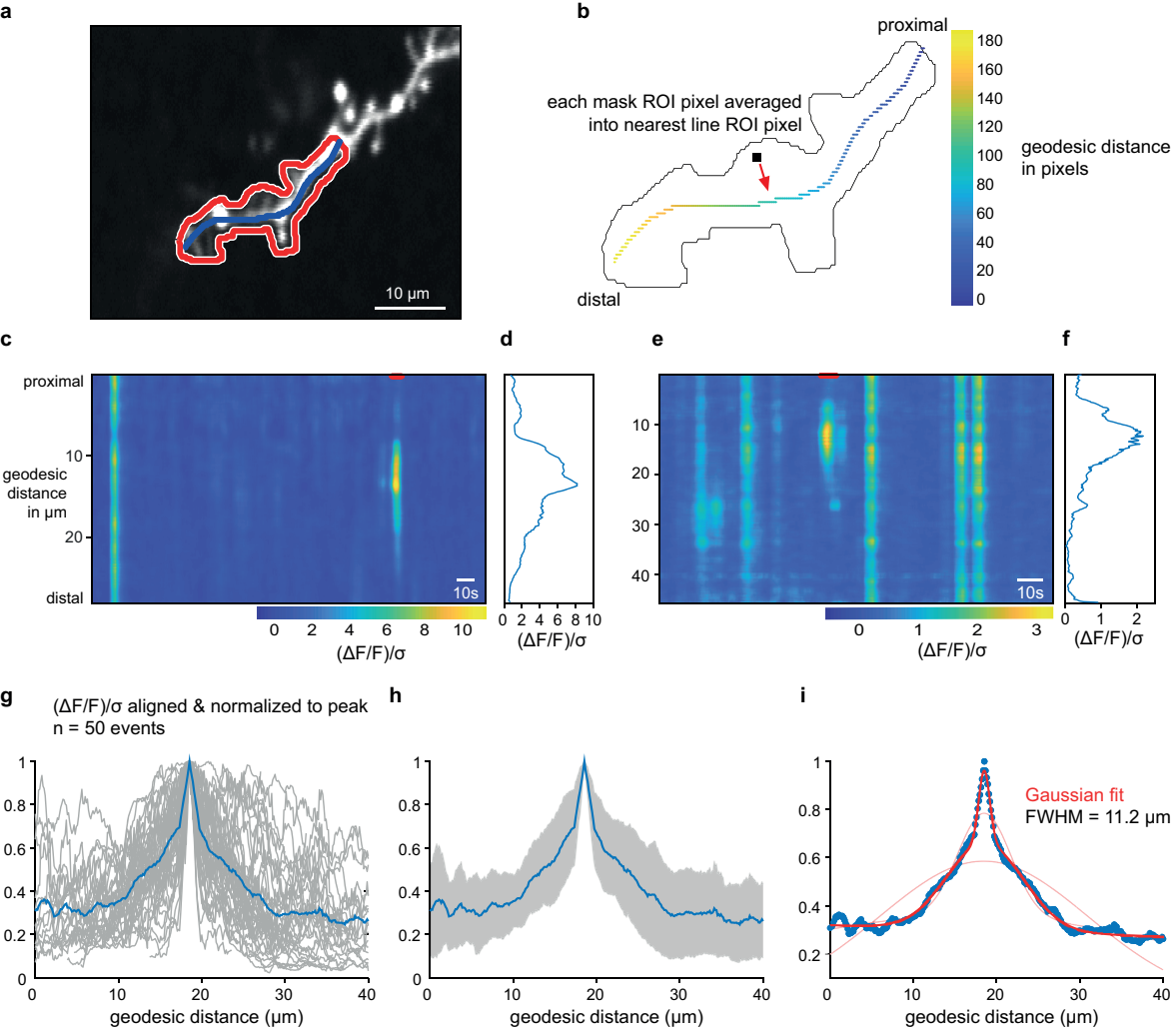
a
10 µm
b
proximal
each mask ROI pixel averaged
into nearest line ROI pixel
distal
180
160
140
120
100
80
60
40
20
0
geodesic distance
in pixels
c
proximal
10
geodesic
distance
in µm
20
distal
10s
0 2 4 6 8 10
(ΔF/F)/σ
d
0 2 4 6 8 10
(ΔF/F)/σ
e
10
20
30
40
10s
0 1 2 3
(ΔF/F)/σ
f
0 1 2
(ΔF/F)/σ
g
(ΔF/F)/σ aligned & normalized to peak
n = 50 events
1
0.8
0.6
0.4
0.2
0
0 10 20 30 40
geodesic distance (µm)
h
1
0.8
0.6
0.4
0.2
0
0 10 20 30 40
geodesic distance (µm)
i
1
0.8
0.6
0.4
0.2
Gaussian fit
FWHM = 11.2 µm
0 10 20 30 40
geodesic distance (µm)

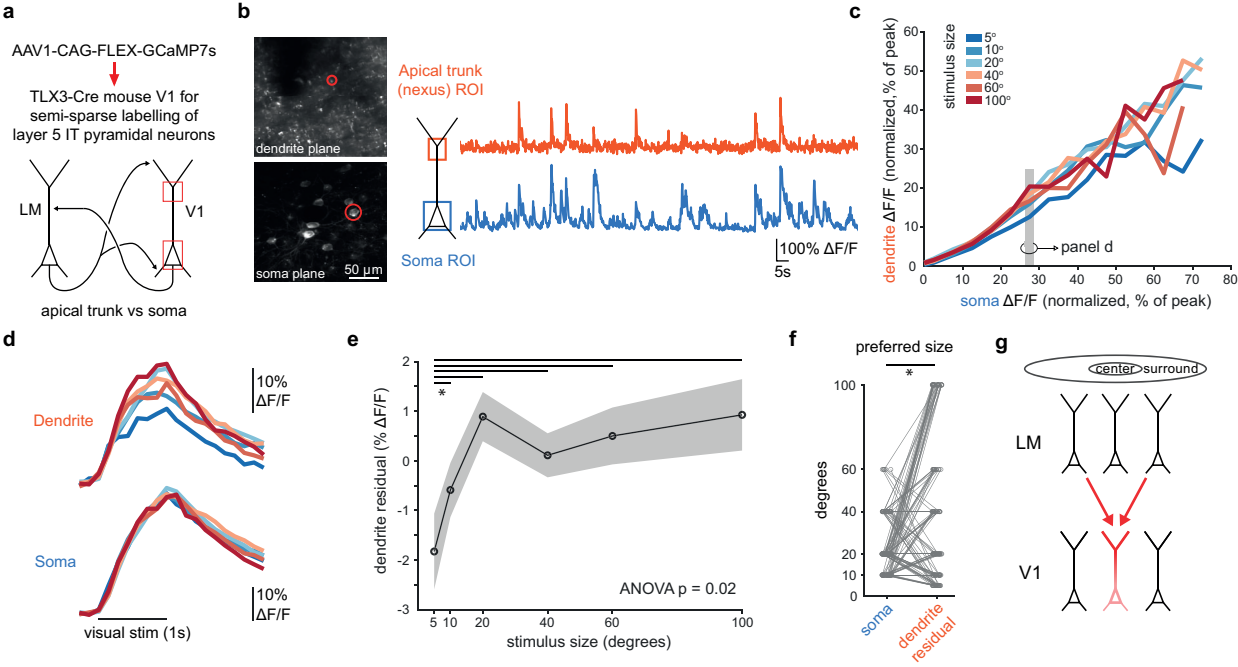
a
AAV1-CAG-FLEX-GCaMP7s
TLX3-Cre mouse V1 for semi-sparse labelling of layer 5 IT pyramidal neurons
LM
V1
apical trunk vs soma
b
dendrite plane
soma plane
50 µm
Apical trunk (nexus) ROI
Soma ROI
100% ΔF/F
5s
c
stimulus size
5°
10°
20°
40°
60°
100°
dendrite ΔF/F (normalized, % of peak)
soma ΔF/F (normalized, % of peak)
panel d
d
Dendrite
Soma
10% ΔF/F
visual stim (1s)
e
dendrite residual (% ΔF/F)
ANOVA p = 0.02
stimulus size (degrees)
f
preferred size
degrees
soma
dendrite residual
g
center surround
LM
V1

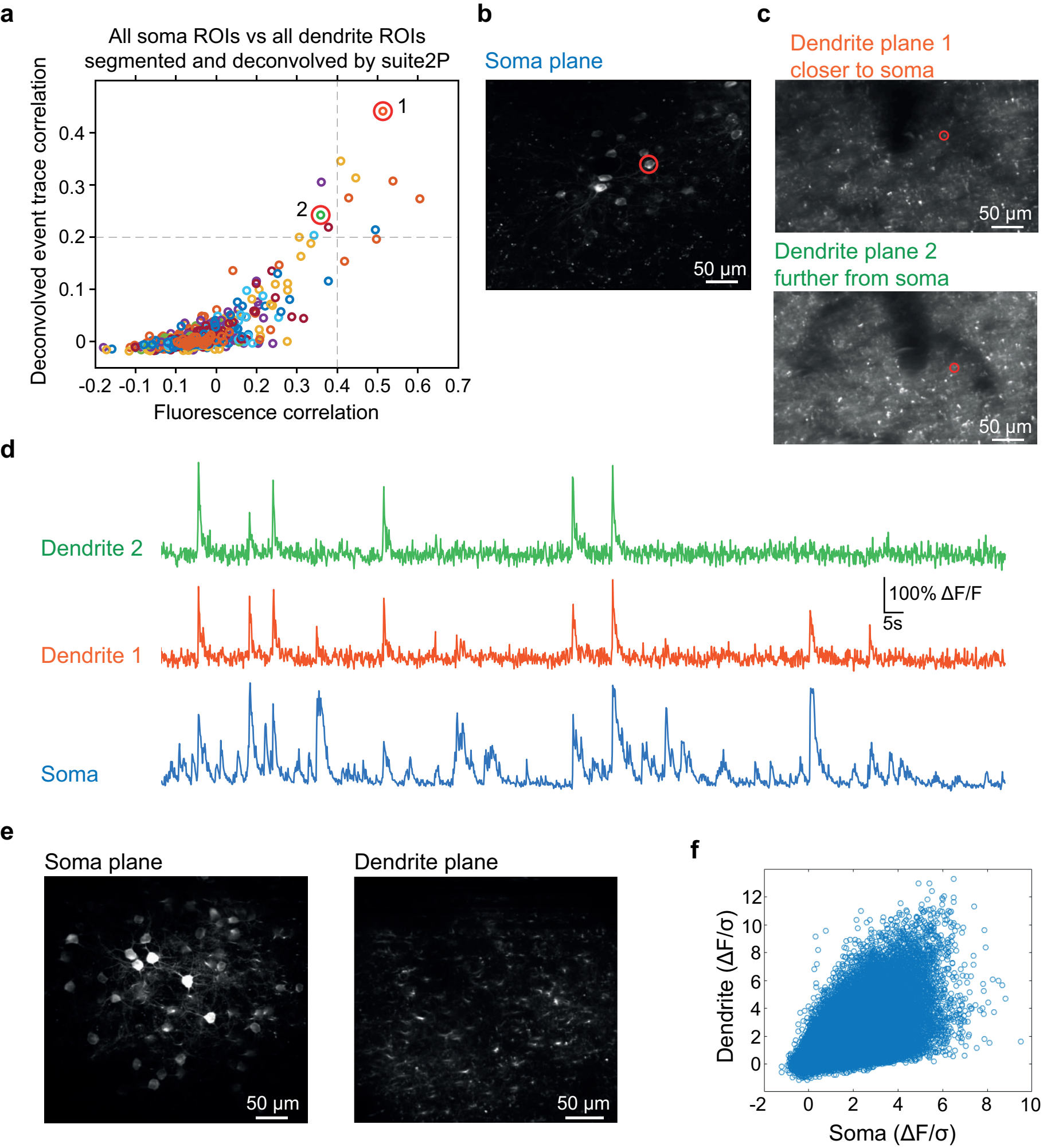
a
All soma ROIs vs all dendrite ROIs
segmented and deconvolved by suite2P
Deconvolved event trace correlation
Fluorescence correlation
1
2
b
Soma plane
50 µm
c
Dendrite plane 1
closer to soma
50 µm
Dendrite plane 2
further from soma
50 µm
d
Dendrite 2
Dendrite 1
Soma
100% ΔF/F
5s
e
Soma plane
Dendrite plane
50 µm
50 µm
f
Dendrite (ΔF/σ)
Soma (ΔF/σ)

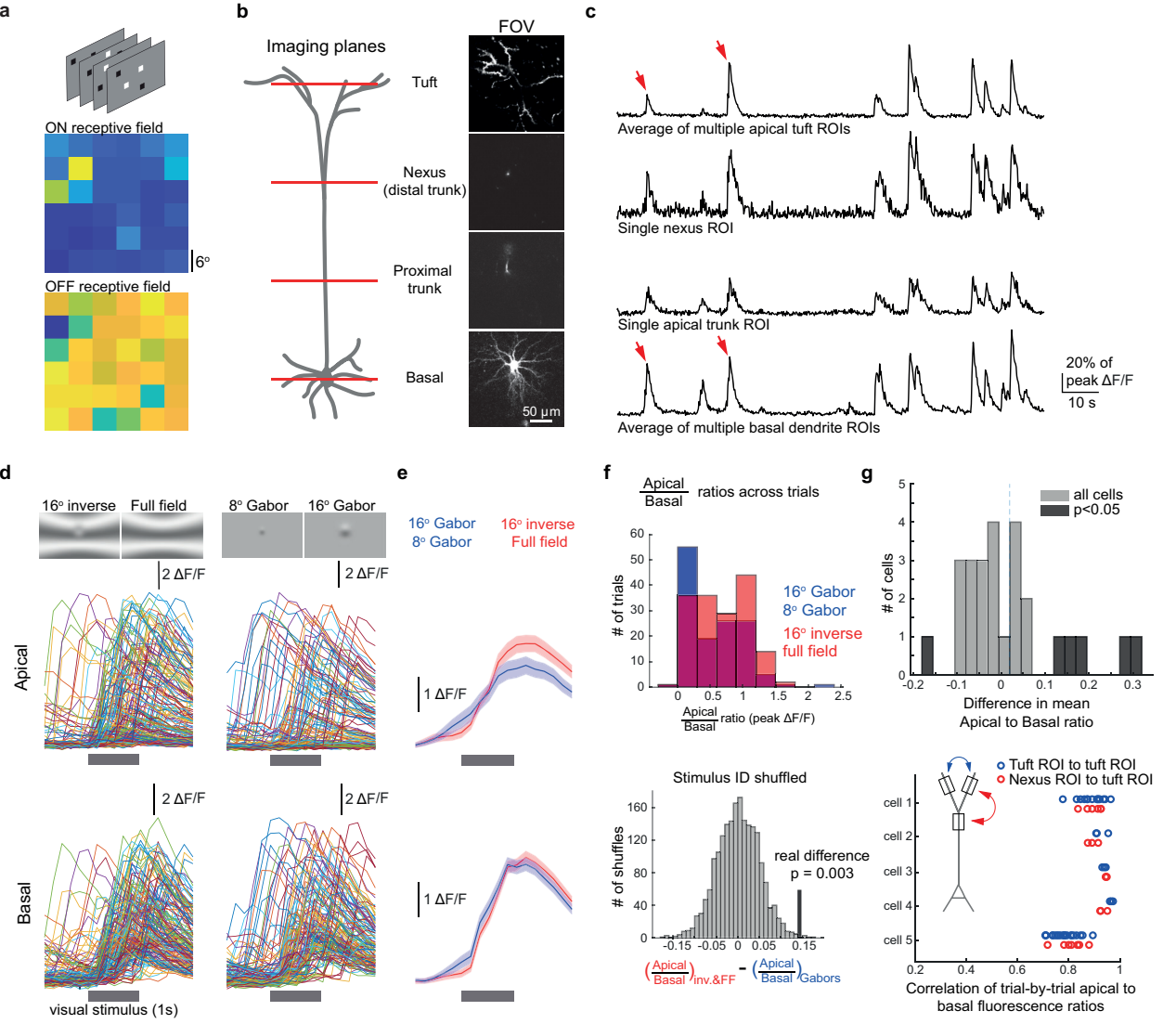
a
ON receptive field
6°
OFF receptive field
b
Imaging planes
FOV
Tuft
Nexus
(distal trunk)
Proximal
trunk
Basal
50 µm
c
Average of multiple apical tuft ROIs
Single nexus ROI
Single apical trunk ROI
Average of multiple basal dendrite ROIs
20% of
peak ΔF/F
10 s
d
16° inverse
Full field
8° Gabor
16° Gabor
2 ΔF/F
Apical
Basal
visual stimulus (1s)
e
16° Gabor
8° Gabor
16° inverse
Full field
1 ΔF/F
f
Apical
Basal
ratios across trials
# of trials
16° Gabor
8° Gabor
16° inverse
full field
Apical
Basal
ratio (peak ΔF/F)
Stimulus ID shuffled
# of shuffles
real difference
p = 0.003
(Apical/Basal)inv.&FF - (Apical/Basal)Gabors
g
all cells
p<0.05
# of cells
Difference in mean
Apical to Basal ratio
Tuft ROI to tuft ROI
Nexus ROI to tuft ROI
cell 1
cell 2
cell 3
cell 4
cell 5
Correlation of trial-by-trial apical to
basal fluorescence ratios

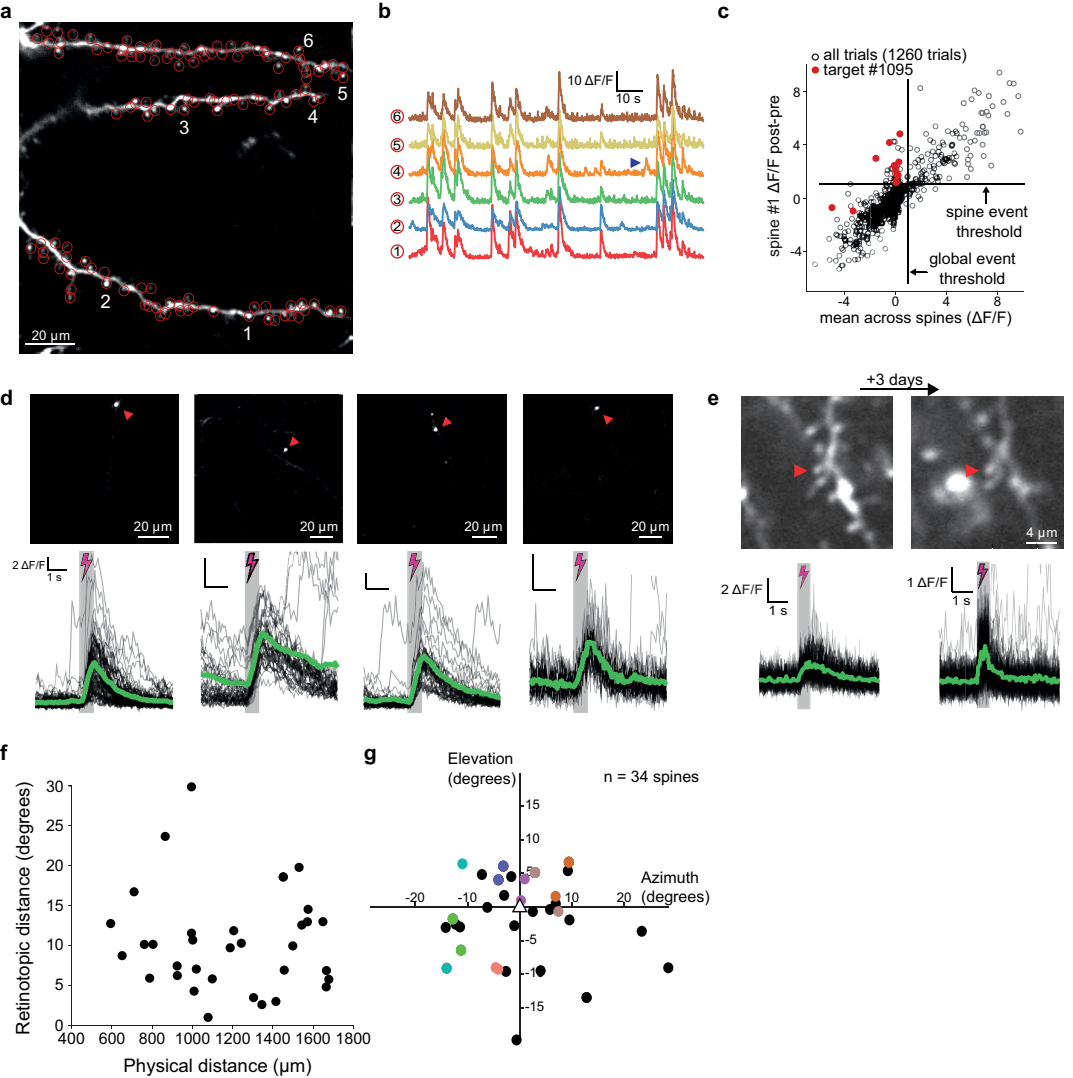
a
6
5
4
3
2
1
20 µm
b
10 ΔF/F
10 s
c
all trials (1260 trials)
target #1095
spine #1 ΔF/F post-pre
mean across spines (ΔF/F)
spine event threshold
global event threshold
d
20 µm
2 ΔF/F
1 s
e
+3 days
4 µm
2 ΔF/F
1 s
1 ΔF/F
1 s
f
Retinotopic distance (degrees)
Physical distance (µm)
g
Elevation (degrees)
n = 34 spines
Azimuth (degrees)

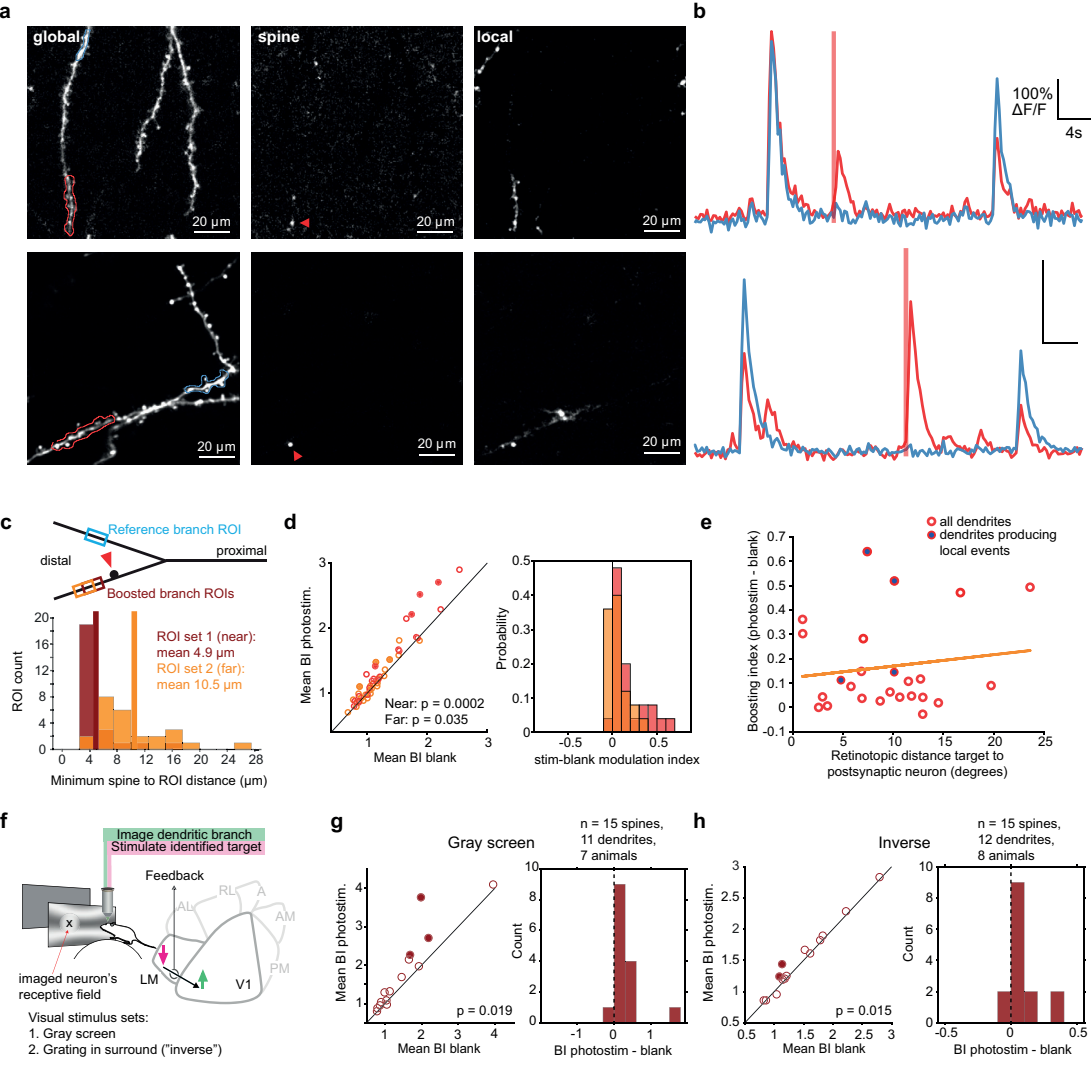
a
global
spine
local
20 µm
b
100%
ΔF/F
4s
c
Reference branch ROI
distal
proximal
Boosted branch ROIs
ROI count
ROI set 1 (near):
mean 4.9 µm
ROI set 2 (far):
mean 10.5 µm
Minimum spine to ROI distance (µm)
d
Mean BI photostim.
Mean BI blank
Near: p = 0.0002
Far: p = 0.035
Probability
stim-blank modulation index
e
all dendrites
dendrites producing local events
Boosting index (photostim - blank)
Retinotopic distance target to postsynaptic neuron (degrees)
f
Image dendritic branch
Stimulate identified target
Feedback
imaged neuron's receptive field
LM
V1
RL
A
AL
AM
PM
Visual stimulus sets:
1. Gray screen
2. Grating in surround ("inverse")
g
Gray screen
n = 15 spines, 11 dendrites, 7 animals
p = 0.019
Count
BI photostim - blank
h
Inverse
n = 15 spines, 12 dendrites, 8 animals
p = 0.015

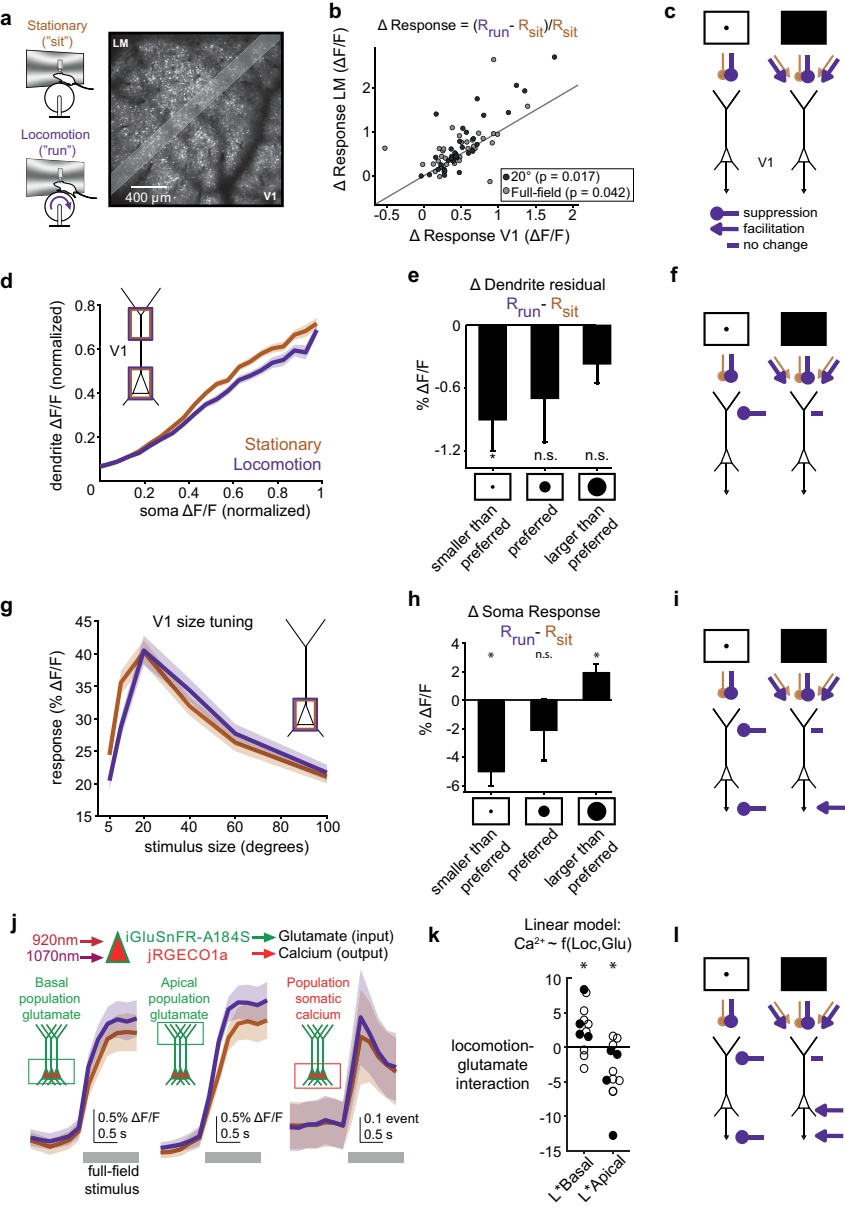
a
Stationary ("sit")
Locomotion ("run")
LM
400 μm
V1
b
Δ Response = (Rrun - Rsit)/Rsit
Δ Response LM (ΔF/F)
Δ Response V1 (ΔF/F)
20° (p = 0.017)
Full-field (p = 0.042)
c
V1
suppression
facilitation
no change
d
dendrite ΔF/F (normalized)
soma ΔF/F (normalized)
V1
Stationary
Locomotion
e
Δ Dendrite residual
Rrun - Rsit
% ΔF/F
n.s.
n.s.
smaller than preferred
preferred
larger than preferred
f
g
V1 size tuning
response (% ΔF/F)
stimulus size (degrees)
h
Δ Soma Response
Rrun - Rsit
% ΔF/F
n.s.
smaller than preferred
preferred
larger than preferred
i
j
920nm
1070nm
iGluSnFR-A184S
jRGECO1a
Glutamate (input)
Calcium (output)
Basal population glutamate
Apical population glutamate
Population somatic calcium
0.5% ΔF/F
0.5 s
0.5% ΔF/F
0.5 s
0.1 event
0.5 s
full-field stimulus
k
Linear model:
Ca2+ ~ f(Loc,Glu)
locomotion-glutamate interaction
L*Basal
L*Apical
l

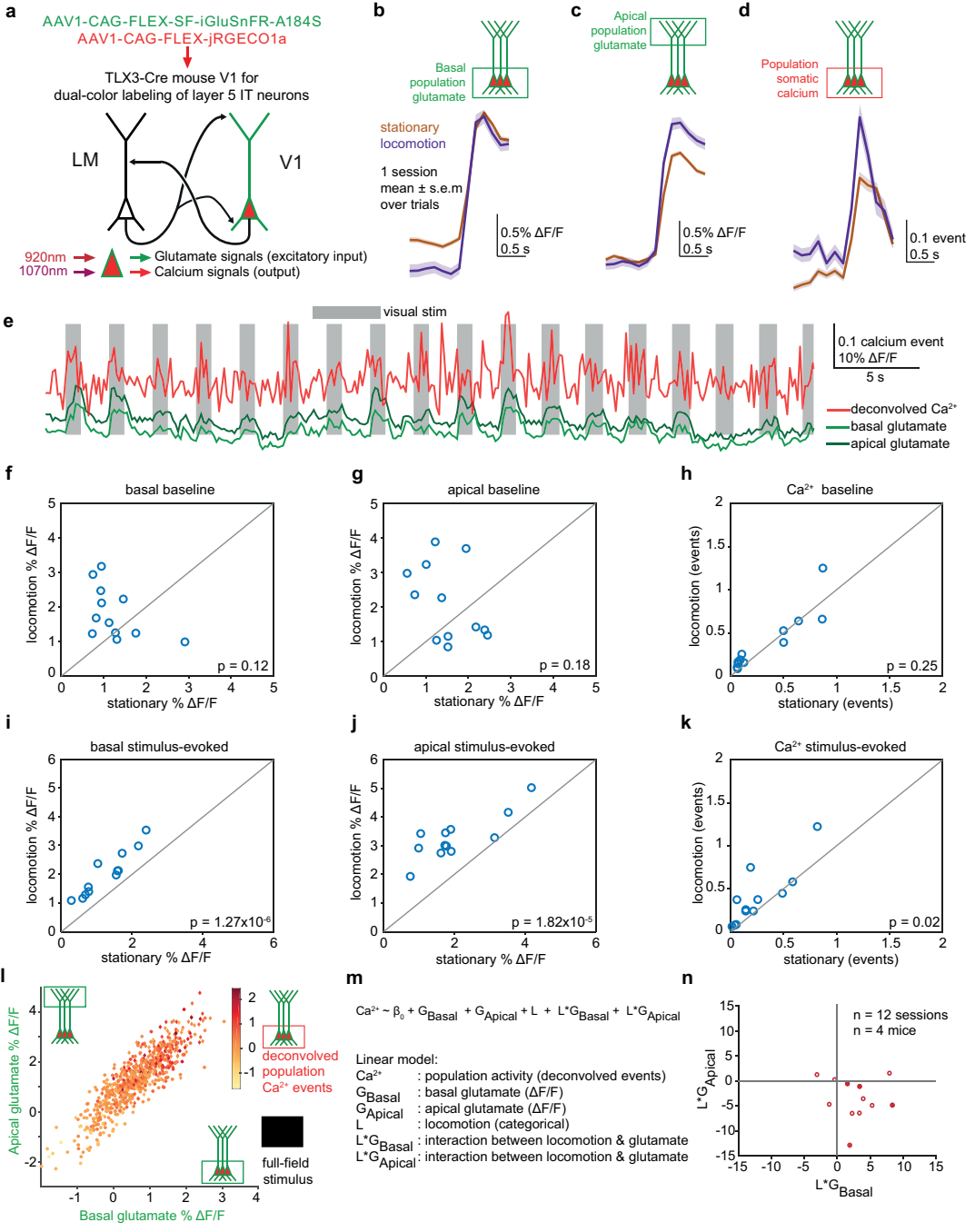
a
AAV1-CAG-FLEX-SF-iGluSnFR-A184S
AAV1-CAG-FLEX-jRGECO1a
TLX3-Cre mouse V1 for
dual-color labeling of layer 5 IT neurons
LM
V1
920nm
1070nm
Glutamate signals (excitatory input)
Calcium signals (output)
b
Basal
population
glutamate
stationary
locomotion
1 session
mean ± s.e.m
over trials
0.5% ΔF/F
0.5 s
c
Apical
population
glutamate
0.5% ΔF/F
0.5 s
d
Population
somatic
calcium
0.1 event
0.5 s
e
visual stim
0.1 calcium event
10% ΔF/F
5 s
deconvolved Ca2+
basal glutamate
apical glutamate
f
basal baseline
locomotion % ΔF/F
stationary % ΔF/F
p = 0.12
g
apical baseline
locomotion % ΔF/F
stationary % ΔF/F
p = 0.18
h
Ca2+ baseline
locomotion (events)
stationary (events)
p = 0.25
i
basal stimulus-evoked
locomotion % ΔF/F
stationary % ΔF/F
p = 1.27x10-6
j
apical stimulus-evoked
locomotion % ΔF/F
stationary % ΔF/F
p = 1.82x10-5
k
Ca2+ stimulus-evoked
locomotion (events)
stationary (events)
p = 0.02
l
Apical glutamate % ΔF/F
Basal glutamate % ΔF/F
deconvolved
population
Ca2+ events
full-field
stimulus
m
Ca2+ ~ β0 + GBasal + GApical + L + L*GBasal + L*GApical
Linear model:
Ca2+ : population activity (deconvolved events)
GBasal : basal glutamate (ΔF/F)
GApical : apical glutamate (ΔF/F)
L : locomotion (categorical)
L*GBasal : interaction between locomotion & glutamate
L*GApical : interaction between locomotion & glutamate
n
n = 12 sessions
n = 4 mice
L*GApical
L*GBasal

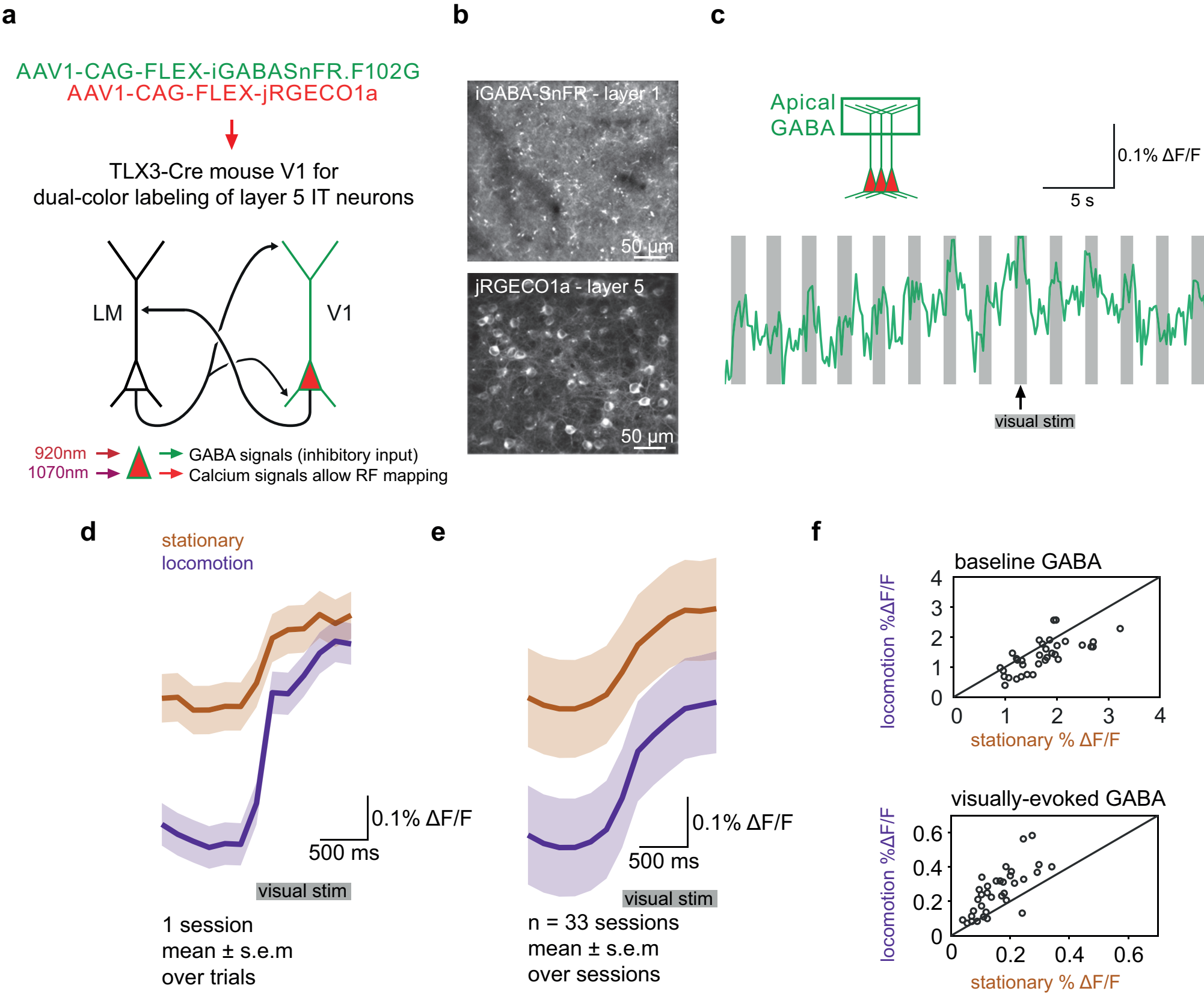
a
AAV1-CAG-FLEX-iGABASnFR.F102G
AAV1-CAG-FLEX-jRGECO1a
TLX3-Cre mouse V1 for
dual-color labeling of layer 5 IT neurons
LM
V1
920nm
1070nm
GABA signals (inhibitory input)
Calcium signals allow RF mapping
b
iGABA-SnFR - layer 1
50 µm
jRGECO1a - layer 5
50 µm
c
Apical
GABA
0.1% ΔF/F
5 s
visual stim
d
stationary
locomotion
0.1% ΔF/F
500 ms
visual stim
1 session
mean ± s.e.m
over trials
e
0.1% ΔF/F
500 ms
visual stim
n = 33 sessions
mean ± s.e.m
over sessions
f
baseline GABA
locomotion %ΔF/F
stationary % ΔF/F
visually-evoked GABA
locomotion %ΔF/F
stationary % ΔF/F